

Final Technical Report

**A COMPACT FREQUENCY AGILE MID-INFRARED
AIRBORNE LIDAR**

**Issued by U.S. Army Aviation and Missile Command under
Contract No. DAAH01-03-C-R115**

**Prepared for
Defense Advanced Research Projects Agency (DOD)
ARPA Order No. N854/46**

**For the period
April 2003—October 2006**

**Submitted by
E.V. Degtiarev, Principle Investigator
LaSen, Inc.
300 North Telshor Blvd., Suite 400
Las Cruces, NM 88011**

Approved for public release; distribution unlimited

Report Documentation Page			Form Approved OMB No. 0704-0188		
Public reporting burden for the collection of information is estimated to average 1 hour per response, including the time for reviewing instructions, searching existing data sources, gathering and maintaining the data needed, and completing and reviewing the collection of information. Send comments regarding this burden estimate or any other aspect of this collection of information, including suggestions for reducing this burden, to Washington Headquarters Services, Directorate for Information Operations and Reports, 1215 Jefferson Davis Highway, Suite 1204, Arlington VA 22202-4302. Respondents should be aware that notwithstanding any other provision of law, no person shall be subject to a penalty for failing to comply with a collection of information if it does not display a currently valid OMB control number.					
1. REPORT DATE 01 OCT 2006		2. REPORT TYPE Final		3. DATES COVERED -	
4. TITLE AND SUBTITLE A Compact Frequency Agile Mid-Infrared Airborne Lidar			5a. CONTRACT NUMBER DAAH01-03-C-R115		
			5b. GRANT NUMBER		
			5c. PROGRAM ELEMENT NUMBER		
6. AUTHOR(S)			5d. PROJECT NUMBER		
			5e. TASK NUMBER		
			5f. WORK UNIT NUMBER		
7. PERFORMING ORGANIZATION NAME(S) AND ADDRESS(ES) LaSen, Inc.			8. PERFORMING ORGANIZATION REPORT NUMBER		
9. SPONSORING/MONITORING AGENCY NAME(S) AND ADDRESS(ES)			10. SPONSOR/MONITOR'S ACRONYM(S)		
			11. SPONSOR/MONITOR'S REPORT NUMBER(S)		
12. DISTRIBUTION/AVAILABILITY STATEMENT Approved for public release, distribution unlimited					
13. SUPPLEMENTARY NOTES					
14. ABSTRACT					
15. SUBJECT TERMS					
16. SECURITY CLASSIFICATION OF:			17. LIMITATION OF ABSTRACT SAR	18. NUMBER OF PAGES 67	19a. NAME OF RESPONSIBLE PERSON
a. REPORT unclassified	b. ABSTRACT unclassified	c. THIS PAGE unclassified			

Disclaimer

The views and conclusions contained in this document are those of the authors and should not be interpreted as representing the official policies, either expressed or implied, of the Defense Advanced Research Projects Agency or the U.S. Government

Abstract

This SBIR project investigated design tradeoffs involved in the construction of a compact mid-infrared lidar suitable for deployment on a small Unmanned Aerial Vehicle (UAV). The prototype sensor assembled under the Phase II program is capable of airborne chemical detection with a sensitivity in the low ppm-m range by means of the infrared differential absorption technique. The system incorporates an optical parametric oscillator (OPO) based laser transmitter capable of random access wavelength tuning in the 3.2—3.5 μm wavelength band at the pulse repetition rate of 100 Hz. Wallplug transmitter efficiency approaches 0.5% with pulse energies of 1 mJ. The prototype system uses a wide-angle 2-inch aperture optical receiver which enables an effective standoff range up to 150 m. Airworthiness of the compact lidar system has been proven in flight tests using a turbine engine helicopter as the airborne platform.

List of Acronyms

ALPIS®	Airborne Lidar Pipeline Inspection System
AOTF	Acousto-Optic Tunable Filter
CPU	Central Processor Unit
DAQ	Data Acquisition
DARPA	Defense Advance Research Projects Agency
DEM	Digital Elevation Model
DIAL	Differential Absorption Lidar
DISC	Differential Scattering
DMA	Direct Memory Access
DoD	Department of Defense
DPSSL	Diode Pumped Solid State Laser
EMSS	Enhanced Mobile Satellite Services
EO	Electro Optic
FCS	Future Combat Systems
FTIR	Fourier Transform Infrared Spectrometer
GIS	Geographic Information System
GPS	Global Positioning System
InSb	Indium Antimonide
IOPPO	Intracavity Optical Parametric Oscillator
IR	Infrared
KTA	Potassium Titanyl Arsenate
KTP	Potassium Titanyl Phosphate
LIDAR	Light Detection and Ranging
LOS	Line of Sight
MANET	Mobile Ad-hoc Networking
Nd:YAG	Neodimium Doped Yttrium Aluminum Garnet
OPO	Optical Parametric Oscillator
OS	Operating System
PPLN	Periodically Poled Lithium Niobate
PRF	Pulse Repetition Frequency
SBIR	Small Business Innovative Research (Program)
TEC	Thermoelectric Coolers
TIC	Toxic Industrial Chemicals
UAV	Unmanned Aerial Vehicle
UT	Universal Time
VOC	Volatile Organic Compounds

Table of Contents

Abstract.....	III
List of Acronyms	IV
List of Figures	VI
List of Tables	VII
1 Introduction.....	1
2 Methods, Assumptions, and Procedures	2
3 Results and Discussion	6
3.1 Mid-Infrared Laser Source.....	6
3.1.1 Pump Laser	6
3.1.2 Laser Cooling System	7
3.1.3 OPO.....	11
3.1.4 Crystal Selection	12
3.1.5 OPO Linewidth Considerations	13
3.1.6 OPO Tuning.....	14
3.1.6.1 Review of the OPO Tuning Methods.....	14
3.1.6.2 Angular Tuning of the OPO.....	17
3.1.6.3 Crystal Mount Design and Moment of Inertia	18
3.1.6.4 Galvanometric Tuner Characteristics	20
3.1.6.5 Accuracy and Adequacy of Position Feedback Signal	22
3.2 Receiver Design.....	23
3.3 Overall System Layout and Parameters.....	24
3.4 Onboard System Controller	26
3.5 Real-Time Communication and Data Reporting	31
3.5.1 Data Types, Bandwidth Requirements Analysis	32
3.5.2 Low-Level Networking, Methods of Wireless Communication.....	34
3.5.3 High-Level Network and Software Architecture.....	37
3.6 System Testing, Calibration and Verification.....	39
3.6.1 System Spectral Calibration:.....	39
3.6.2 Ground-based system testing	41
3.6.2.1 Ground-Based Testing: Methane	41
3.6.2.2 Ground-Based Testing: Diesel Vehicle Emissions.....	43
3.6.3 Airborne Testing.....	44
3.7 Mid to Near Infrared Up-Conversion Demonstration.....	47
3.7.1 Background.....	47
3.7.2 Optical Design of the Up-Converter	48
3.7.3 Conversion Efficiency	50
3.7.4 Up-Converter Solid Acceptance Angle	51
3.7.5 Up-Converter Spectral Acceptance Bandwidth.....	54
3.7.6 Pulsed Mid-IR Optical Up-Converter Experiments.....	56
3.7.6.1 Experimental Setup.....	56
3.7.6.2 Black Body Up-Conversion Tests	57
4 Conclusions.....	59
References.....	60

List of Figures

Figure 1. DIAL and DISC lidar principle.	3
Figure 2. Diode pumped solid-state laser head.	7
Figure 3. Compact cooler block diagram.	9
Figure 4. External (a) and internal cavity (b) OPO configurations.	11
Figure 5. KTA tuning curve. Phase-matching in the xz-plane. (1) idler wave,	13
Figure 6. LaSen's mid-infrared OPO/tuner design based on an intracavity AOTF.	16
Figure 7. Opto-mechanical angular tuner used in LaSen's Lidar II system.	17
Figure 8. A high speed OPO angular tuner using a galvanometric scanner.	18
Figure 9. Mechanical design of the KTA crystal mount.	19
Figure 10. Receiver optical layout.	24
Figure 11. Overall system layout.	25
Figure 12. Onboard controller architecture.	30
Figure 13. Lidar controller timing diagram. (a) analog input gate of the DAQ cards, (b) galvanometer advance, (c) laser diode current gate, and (d) Q-switch gate. Curve (e) shows a typical signal waveform.	31
Figure 14. Data exchange overview.	32
Figure 15. Communications architecture for airborne lidar.	37
Figure 16. Compact airborne lidar network structure.	38
Figure 17. Sample report demonstrating layered presentation of various types of data by GIS software.	39
Figure 18. Methane absorption spectrum through a 270 ppm-m absorption cell as a function of raw galvanometer position counts.	40
Figure 19. Spectral calibration function.	40
Figure 20. Transmission of a 100-m long path containing 1.7 ppm concentration of methane and 20000 ppm concentration of water.	42
Figure 21. Transmission spectrum of diesel truck emissions (blue) and neat diesel fuel in a calibration cell (red).	43
Figure 22. Helicopter flight path superimposed on the area map. A red flag symbol marks the point of methane release.	45
Figure 23. Differential absorption signal in the methane release test. X—pulse number, Y—differential absorption ratio.	46
Figure 24. Visual (right) and infrared (left) images of a 100-scfh methane release.	46
Figure 25. Up-converter optical layout.	49
Figure 26. Tangential phase matching geometry in lithium niobate.	52
Figure 27. Phase mismatch as a function of the infrared angle deviation.	54
Figure 28. Spectral acceptance bandwidth of a lithium niobate up-converter.	55
Figure 29. Optical layout of the up-conversion experiment.	56
Figure 30. Up-converter mechanical layout.	57
Figure 31. Spectral tuning of up-converted radiation from a black body source. The pump beam external angle is θ . (1) $\theta = 11^\circ$, (2) $\theta = 5^\circ$, (3) $\theta = 4^\circ$	58

List of Tables

Table 1. Optical properties of the KTA crystal.....	12
Table 2. Calculated moment of inertia of KTA and mount assembly	19
Table 3. Step-and-settle tuning response for the LBS-6124 galvanometer.	20
Table 4. The maximum frequency of motion for LBS-6124 galvanometer.	21
Table 5. Comparison of various system standards.....	28
Table 6. Lidar data package.	33
Table 7. Comparison of common streaming video compression methods.	33
Table 8. Specifications of NovaRoam ED900TM.....	35
Table 9. Performance of NovaRoam ED900TM.	35
Table 10. Specifications of satellite module for ICS by Level 3 communications.....	36
Table 11. Specifications of Iridium 9505 satellite terminal.....	36

1 Introduction

The military technology of today would be unimaginable without a multitude of electro-optical (EO) sensors. From laser rangefinders to night vision goggles and thermal infrared imagers, electro-optical devices perform a number of crucial functions on the modern battlefield. It is safe to predict that the military use of EO technology will only expand in the future.

Of particular interest for future combat and reconnaissance missions is an emerging class of electro-optical sensors which ascertain chemical composition of battlefield objects by performing what is essentially a remote spectroscopic measurement. A general principle of spectroscopy is that light waves reflected, transmitted or emitted by an object carry its unique fingerprint (called spectrum). Thus, by analyzing light received from the object, it is possible to ascertain, in many cases remotely, the object's chemical composition.

Chemical EO sensors can generally be classified as passive or active depending on whether or not the sensor contains an illumination source. Passive sensors, such as Fourier Transform Infrared Spectrometers (FTIR) and hyperspectral imagers, employ the naturally occurring background radiation and self radiance of objects. In contrast, the active sensors provide an independent illumination source typically in the form of laser radiation.

The active laser-based sensors typically operate in one of the two regions of the infrared (IR) spectrum: mid-wave IR (3—5 μm) and long-wave IR (8—12 μm). The mid-IR range is spectroscopically significant due to the fact that frequencies of absorption transitions associated with C-H, O-H and N-H bonds fall into this range. Since these types of bonds are ubiquitous in organic compounds, both natural and man-made, the mid-IR region provides access to a number of important military targets, including various paints and coatings, fumes, engine emissions, chemical and biological warfare agents.

The Future Combat Systems (FCS) will greatly benefit from a chemical remote sensor that combines the power of infrared laser sensing technology with the mobility of an Unmanned Aerial Vehicle (UAV) platform. Such a sensor will provide a persistent look at the battlefield, aiding in the detection and identification of targets and threats, while performing these functions from a safe standoff distance.

The Phase II SBIR effort was to evaluate the potential for a mid-IR airborne chemical sensor compatible with the payload requirements of a small UAV. Such a task poses a number of technical challenges that were addressed in the present research. The biggest challenge is to manage mechanical (weight and size) and electrical (power consumption) overhead associated with generating sufficient laser power in the IR.

Requirements on the transmitted laser power can be conceivably alleviated if the system's detector is improved. To this end, a secondary effort under the DARPA project was to evaluate a particular optical technique that promises an increase in the sensitivity of infrared signal detection.

2 Methods, Assumptions, and Procedures

The military action following the events of Sept. 11, 2001 has put intelligence, surveillance and reconnaissance in the spotlight. It has highlighted the need to persistently monitor the battlefield to locate enemy targets by day or by night. The U.S. adversaries have become more successful in developing not only unique methods of destruction, but also more sophisticated means of eluding detection. Presently, there exists an acute need for tactical reconnaissance and airborne surveillance technologies that can overcome camouflage, concealment and deception [1].

The rapidly increasing use of Unmanned Aerial Vehicles (UAVs) makes them attractive platforms for deployment of airborne reconnaissance sensors. The remote command and control capability offered by these systems eliminates the need to put a human operator into harm's way. A number of UAVs presently exist, both domestically and internationally. Their payload weight carrying capability, their accommodations (volume, environment), their mission profile (altitude, range, duration) and their command, control and data acquisition capabilities vary significantly. While high performance platforms such as the RQ-1 Predator can carry a payload of up to 450 pounds, they also have a significant cost (in the tens of millions of dollars range) associated with them [2]. Therefore, the sensors deployed on the high performance UAVs may be limited to long-range operation from the target in order to stay outside the range of the enemy's weapons.

On the other hand, an increasing number of smaller, far less expensive UAVs have become available in recent years, and more of such platforms continue to appear on the market [3]. The payload capability of these systems is typically in the few pounds to tens of pounds range with the price starting well under \$100K. The relatively low profile and cost of these platforms will allow them to penetrate deeper into hostile airspace and interrogate potential targets from a closer range. A network of deployed sensors can provide a persistent and comprehensive coverage of the battlefield, satisfying the need for information by day or night.

Remote sensing in the infrared can greatly increase the capabilities of tactical airborne reconnaissance systems. By processing information from a wider range of the electro-magnetic spectrum than the one accessible to human eye, infrared remote sensors can assess such target properties as thermal state, chemical composition and volatile emissions. When the full power of optical remote sensing is brought to bear, the enemy's possibilities for evasion of detection are drastically reduced.

Laser based (active) remote sensing technologies have distinct advantages over the passive ones. For example, observation using an active system is not dependent upon object emissivity, temperature or on external natural illumination, as is the case with a passive sensor. Also, conventional passive sensors frequently rely on geometrical shape for target recognition. In contrast, an active multi-spectral sensor would use the spectral characteristics of the target. This could be particularly advantageous in situations where the target is heavily concealed and could also significantly decrease the sensor spatial resolution requirements. Well-established, exploitable phenomenology, reduced sensitivity to ambient illumination levels and lowered spatial resolution requirements all combine to make active multi-spectral sensing an attractive candidate for finding and identifying heavily concealed targets.

A number of physical mechanisms can be used as the basis for laser-based chemical remote sensing. Of these, differential absorption lidar (DIAL) and differential scattering (DISC) offer the highest sensitivity due to the strongest material response. Other laser-based techniques, such as fluorescence and Raman spectroscopy have orders of magnitude less sensitivity.

Any lidar system consists of two major parts: transmitter and receiver (Figure 1). The transmitter is typically a laser or laser-based source of optical radiation. Light generated by the transmitter is emitted into the atmosphere as a collimated beam. As this beam propagates away from the source, some of the radiation will be scattered back toward the receiver by objects in the beam path or by the atmosphere itself due to Rayleigh and Mie processes. Additionally, light waves will interact with molecules of chemicals present in the beam path. These interactions can attenuate the intensity of light (absorption) or change its frequency (inelastic scattering). In either case, the properties of light returning to the receiver will be changed in a unique way. The receiver usually incorporates a large collecting optic, which focuses the backscattered light onto a sensitive detector. Knowing the physical laws that govern scattering and absorption processes, it is possible to make a remote quantitative measurement of chemical concentrations by analyzing the properties of collected light.

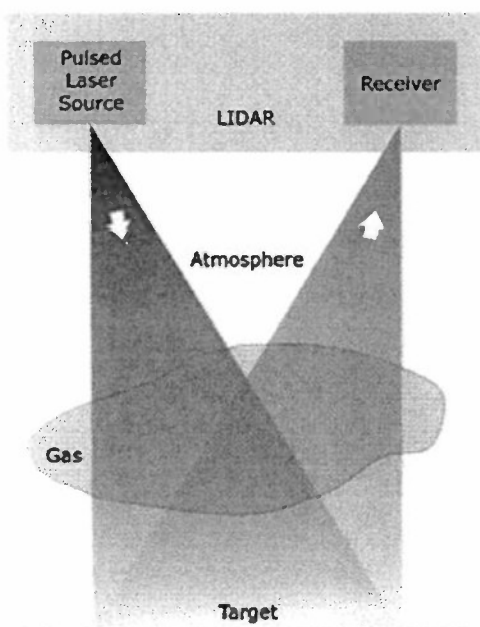


Figure 1. DIAL and DISC lidar principle.

In the DIAL method, the transmitter generates light pulses at two optical frequencies. One frequency, the so-called "on-line", is chosen to coincide with a particular absorption line of the chemical of interest. The other frequency called the "off-line" is tuned away from the absorption peak and serves a reference. If the two frequencies are spaced closely enough, then they are completely equivalent except for the way they interact with specific molecules. When the return energy at the on-line and off-line is compared, a lesser energy of the on-line signal would indicate the presence of a particular chemical in the area interrogated by the beam. More precisely, the logarithm of the ratio of energy returns at the on- and off-lines is representative of

the chemical concentration in the beam path. Due to the high signal strength, the DIAL technique has superior sensitivity compared to fluorescence and Raman lidars. For DIAL detection of hydrocarbons, including volatile organics, the 3—5- μm spectral region is particularly attractive as many molecules have strong and well defined absorption features in this region.

Laser-based remote chemical sensors typically operate in one of the two atmospheric transmission windows: the mid-wave IR (3—5 μm) and long-wave IR (8—12 μm). Typically, a laser sensor can cover a smaller subset of the transmission region depending on the tuning band of the laser source. This inevitable reduction in spectral coverage is more than compensated for by the far superior spectral resolution which translates directly into detection and discrimination capability. Depending on the design, the resolution of active sensors as determined by the laser linewidth can be anywhere from a few wavenumbers to a fraction of a wavenumber.

The principal laser source for the long-wave IR region is the venerable CO_2 laser. This laser can be conveniently tuned over a discrete set of emission lines covering the long-wave IR region. However, due to its large size, weight and power consumption, the CO_2 laser does not lend itself to applications demanding lightweight and compact devices. The solid state laser technology for generating long-wave IR is still immature and usually involves a two stage conversion process, which decreases the overall device efficiency dramatically.

On the other hand, the 3—5- μm region is readily accessed with optical parametric oscillator (OPO) based laser sources. In recent years, the interest in mid-IR OPOs has been burgeoning due to the advent of new nonlinear conversion crystals, pumping sources and tuning mechanisms. A plethora of OPO devices has been demonstrated, ranging from ultra-compact microchip-type devices to the powerful multi-watt systems [4,5]. The efficiency and parameters of mid-IR OPOs are continuously improving, while their cost is steadily decreasing.

The utility of the mid-IR spectral region goes far beyond the availability of an efficient laser source. It is undisputedly the region of choice for the detection of volatile organic compounds (VOCs) and Toxic Industrial Chemicals (TICs) via the differential absorption method. Due to the uniqueness of absorption signatures, the mid-IR spectral region is frequently referred to as the “fingerprint region” for VOCs. Emissions from running engines, fuel and oil spills, effluents from facilities involved in storage and production of chemical and biological weapons are all prime candidates for detection in the mid-IR.

Chemical warfare agents are also known to possess mid-IR signatures. Although spectral data pertaining to the agents themselves is not available in open literature, a correspondence has been established between the spectral properties of chemical agents and their simulants [6]. Based on this correspondence, we can state that a number of chemical warfare agents possess unique spectral signatures in the mid-IR which can be exploited for their detection and identification.

A less recognized fact is that the mid-IR region also has utility in detecting aerosolized biological agents through differential scattering. Conventionally, the long-wave IR region is considered the primary region for bio detection. However, in a study conducted by Lawrence Livermore National Laboratory (LLNL), a mid-IR frequency agile lidar (FAL) has been successfully used to discriminate between biological and non-biological aerosols [7]. In a similar

experiment, LaSen has recently used its compact mid-IR chemical sensor (Lidar II) at the Edgewood Chemical and Biological Center (ECBC) aerosol test facility and the results were in agreement with the LLNL data.

From the foregoing discussion it is clear that a mid-IR active multi-spectral sensor can perform a number of functions critical to current and future DoD missions. Such a sensor deployed on a small UAV can provide a relatively inexpensive and effective means of monitoring the battlefield, gathering intelligence information, locating and cueing various targets. Unfortunately, the mid-IR active sensor technology suitable for deployment on small UAVs does not exist at present.

The greatest challenge in deploying a mid-IR laser sensor on a small UAV is to match the sensor's operational characteristics to the platform's payload capability. To perform any of the above functions in a complex battlefield environment, the sensor must acquire and process information at a high rate, requiring thousands of laser pulses to be fired each second. A high repetition rate laser inevitably generates significant amounts of waste heat that must be disposed of properly. Liquid cooling systems conventionally used for high-repetition rate lasers are often bigger and heavier than the equipment being cooled. The cooling requirement can be alleviated at the expense of reduction of the output power; however, this could in turn limit the system's range and sensitivity. A careful analysis and optimization of all the sub-systems is required to make the technology viable for small UAVs without compromising the performance.

Leveraging from LaSen's extensive experience in building compact, airworthy laser remote sensors, under the Phase II DARPA SBIR program we developed a prototype compact mid-IR active sensor that has the potential for future integration onto small UAV platforms. The resulting sensor achieves a high-speed mid-IR frequency agility in a small weight, size and power envelope, making it suitable for a large number of potential airborne platforms. We anticipate the production cost of the sensor to be under \$150K, which is comparable to the cost of passive airborne sensors employed today.

3 Results and Discussion

3.1 Mid-Infrared Laser Source

Lasers have long since become standard items in a large number of military systems. Modern target designators, communications networks and rangefinders (to name just a few examples) all employ lasers. However, the laser technology required for a remote chemical sensor is significantly different from conventional military grade lasers. The biggest difference is in the fact that chemical sensing requires the laser source to be tunable, i.e., it must have the capability to shift the frequency of the output radiation over a relatively wide spectral range. Furthermore, frequency changes must be accomplished in a short time interval, typically no more than a few milliseconds. Such properties are collectively referred to as frequency agility.

If we combine the frequency agility characteristic with other properties expected in a military grade laser system such as ruggedness, compactness and efficiency, one ends up with a daunting engineering task. The scope of the DARPA project with its emphasis on the overall system engineering aspect did not permit us to investigate drastically new approaches to laser design, such as high power infrared semiconductor lasers. Instead, under this project we evaluated the state-of-the-art design options for tunable mid-IR laser sources.

One approach that has long been recognized for its utility in producing widely tunable infrared radiation uses the principle of Optical Parametric Oscillator (OPO). The OPO is a nonlinear optical device that converts the beam of a fixed-frequency pump laser into two secondary beams called signal and idler whose frequencies can be adjusted (tuned) by various means. This is currently the only mature technology for producing widely-tunable, moderate average power coherent infrared radiation, albeit at the expense of a relatively low overall conversion efficiency.

3.1.1 Pump Laser

The choice of pump laser is driven by the wavelength, efficiency and design considerations. Under the DARPA project, we have opted for Neodimium-doped Yttrium Aluminum Garnet (Nd:YAG) diode-pumped solid state laser technology (DPSSL). These lasers are widely used commercially, which makes them affordable, readily available and easily configurable to meet the specific needs of an R&D project. The Nd:YAG material's primary laser transition is at 1064 nm and the strongest absorption band is centered at 808 nm. One of the biggest advantage of the Nd:YAG laser material is that it can be directly pumped by high power semiconductor laser diodes. Thanks to diode pumping, the Nd:YAG laser provides reasonable electrical-to-optical efficiency (around 20%) even without meticulous optimization.

Our pump laser uses a custom built DPSS laser head from Paradigm Lasers, Inc. (Figure 2). The Nd:YAG crystal is shaped as a cylindrical rod with dimensions of 3 mm × 63 mm. The pump semiconductor laser arrays encircle the rod in a sleeve-like configuration, which ensures a symmetrical pattern of laser gain. This is the radial pumping configuration which the

manufacturer considers proprietary. The body of the laser head is made out of delrin plastic to ensure electrical isolation. The head has electrical connections for drive current and input/output ports for the liquid cooling system.

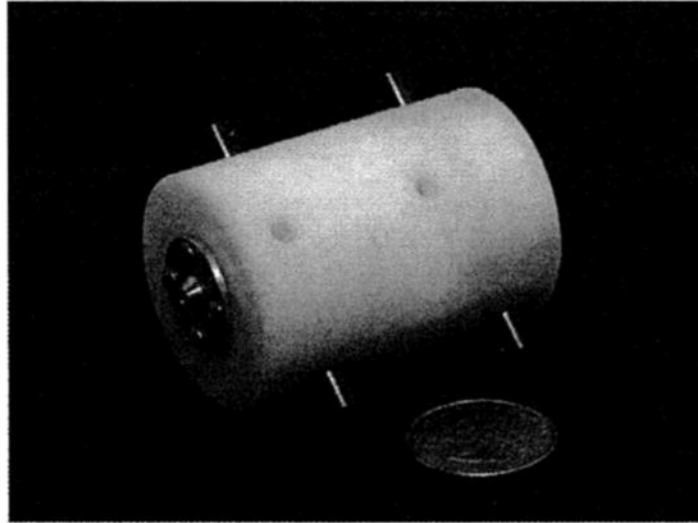


Figure 2. Diode pumped solid-state laser head.

3.1.2 Laser Cooling System

Due to the large heat dissipation requirements of the Nd:YAG laser head, it was determined that an active liquid cooling system was needed for the prototype compact airborne lidar system. Several cooling options were analyzed, taking into consideration: (a) heat dissipation load, (b) power consumption, (c) weight, (d) dimensions, (e) mechanical vibration, (f) anticipated environmental conditions in the field, and (g) FAA requirements. Two primary cooling techniques were considered: vapor compression refrigeration and thermoelectric.

Cooling systems based on vapor compression refrigeration principles are generally more efficient. They are also better suited for operation in hot weather conditions due to a high heat dissipation efficiency even when the heat exchanger is very hot (more than 100 °C). Additionally, some commercial off the shelf (COTS) models currently available can, with certain modifications, be used in the system. However, COTS units that meet all of the requirements listed above are not readily available. A major disadvantage of a vapor compression refrigeration cooling system is the strong mechanical vibration of the (diaphragm) compressor unit. This vibration makes the integration of the cooler into the lidar package extremely difficult. A new type of compact vapor compression refrigeration cooler was recently developed, which is based on a rotary pump. These pumps are virtually free of vibration when compared to that normally associated with a diaphragm pump. Unfortunately, these types of units are generally not available for non-military applications at this time, but will be considered for future development as they do become available.

Thermoelectric-based coolers are less efficient and consume substantially more current to drive their Peltier elements (typically 20—30 A). Also, the operational temperature of the thermoelectric elements cannot exceed a critical point (approximately 75 °C), above which the elements become irreparably damaged. This severely limits their heat dissipation efficiency in hot weather conditions. Additionally, their cooling efficiencies drop almost linearly as ambient temperature rises. As a result they are more suitable to operation in cooler weather conditions. However, thermoelectric coolers do have significant advantages over their vapor compression refrigeration cooler counterparts. They are very compact and they operate very quietly, which is very beneficial in a laser system. After a very thorough analysis of both types of cooling devices, we decided that a compact unit based on thermoelectric coolers would be the best option.

After evaluating the various requirements, a set of cooler specifications was determined. The cooler must be capable of dissipating and removing up to 120 W of heat. This includes approximately 80 W of heat generated by the laser head diodes when running at maximum repetition frequency, and approximately 40 W of parasitic heat added to the coolant from the cooling pumps themselves. The cooler must be able to provide a coolant flow rate through the laser head of at least 1 GPM. The cooler must also be able to maintain a preset temperature (± 0.1 °C) while operating in an environmental ambient temperature range of 0 to 35 °C. The unit is to be powered by the helicopter's on-board 28-V bus (no voltage converters are allowed) with a maximum current load, under the hottest of conditions, not to exceed 13 A.

In order to meet the above requirements and specifications and to ensure that the system is optimized for best performance, numerous tests and experiments had to be performed to determine the best layout configuration and selection of parts and components. A simplified block diagram of the compact liquid cooler is shown in Figure 3.

The primary loop is designed to remove heat from the laser head and transfer it to the heat exchanger. The loop consists of a coolant reservoir tank (T1), a high pressure (30 ft head) 1.5-GPM centrifugal pump (P1), a 15-micron 80-cm² large area filter (F) to remove small particulates, a 0.5-GPM safety flow switch (FS) which disables the laser in the event of a cooling system failure and prevents damage to the laser head, the laser head (L), and the primary cold plate (C1) of the heat exchanger assembly. The loop is also thermally insulated from the ambient air in order to better provide temperature stabilization for the laser head. Additionally, no part of the primary loop that comes in contact with the coolant contains aluminum or brass, which might corrode and damage or destroy the laser head.

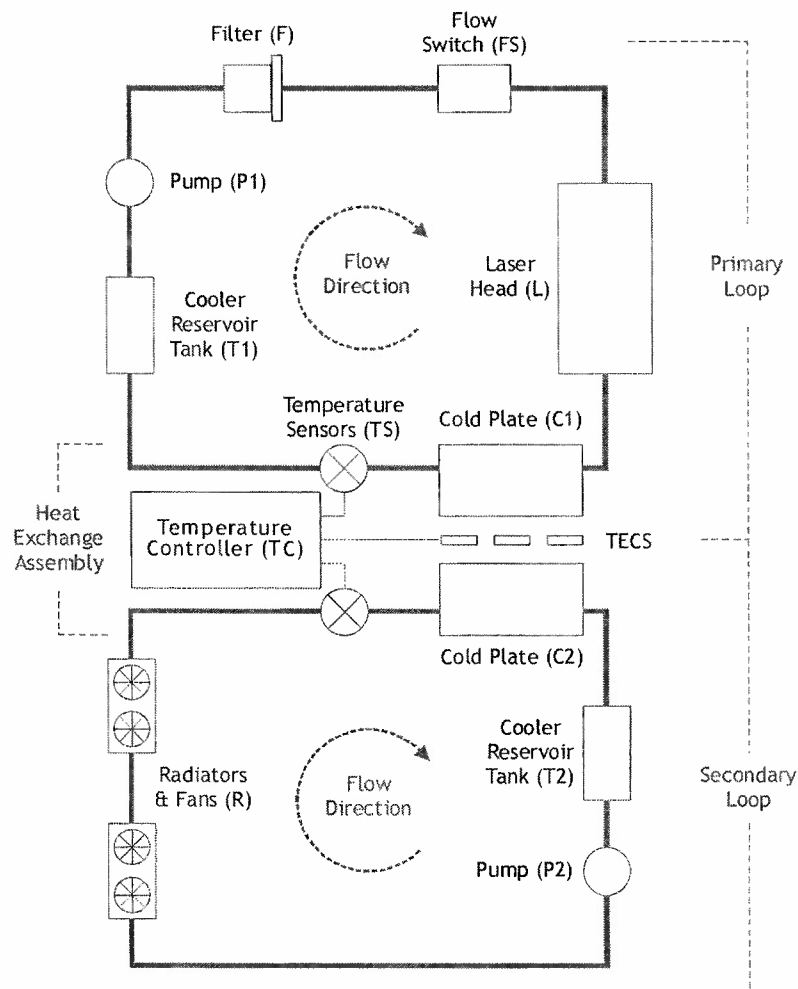


Figure 3. Compact cooler block diagram.

The secondary loop is designed to remove the heat from the heat exchanger and transfer it to the ambient environment. The loop consists of the coolant reservoir tank (T2), a centrifugal pump (P2), a radiator assembly (R) that also mounts four 40-CFM encapsulated fans to ensure proper airflow through the radiator assembly, and the secondary cold plate (C2) of the heat exchanger assembly.

The heat exchanger assembly is designed to transfer the heat from the primary loop and place it into the secondary loop. It consists of the primary (C1) and secondary (C2) cold plates, and six potted thermoelectric coolers (TECs), sandwiched between the two cold plates. The primary cold plate (C1) is a 4-pass copper tubing / aluminum block with a thermal resistance of $0.02\text{ }^{\circ}\text{C/W}$ (at 0.75 GPM) and has a pressure drop of 2 psi at a flow rate of 1 GPM. The secondary cold plate (C2) is a 6-pass copper tubing / aluminum block with a pressure drop of 9 psi at 1 GPM. The TECs are controlled by a temperature controller, which is based on a PIC16 micro-controller, that provides proportional bandwidth, integral gain, and derivative gain (PID) control with a pulse width modulated (PWM) output. It uses a thermistor temperature sensor to provide a stable and minimal temperature variation ($\pm 0.1\text{ }^{\circ}\text{C}$) of the coolant. The TEC resistance and circuit

configuration was optimized to draw a current load of no more than 7 A (at 28 V) while under a 100% load and while keeping the individual current through each TEC at about 75% of their critical current (I_c), where TEC performance is optimal. Additional TEC protection against overheating was achieved by using a secondary control sensor attached to the hot side of the heat exchanger. The working temperature of the coolant was set to 26 °C in accordance with laser diode manufacturer's recommendations. The system can automatically provide both cooling (in hot weather conditions) and heating (in cold weather conditions) without user intervention.

Two different types of coolants are used for each loop. In the primary loop, a perfluorocarbon fluid is used since the laser head diodes are not designed to come into contact with water. This fluid provides excellent flow and heat transfer characteristics and will not damage or corrode any of the parts or components in the loop. In the secondary loop, a mixture of distilled water and additives are used to prevent corrosion and the build up of deposits that may reduce cooler efficiency, and to prevent freezing in the loop since the loop is exposed to the outside ambient environment and may be subject to freezing conditions when cold air temperatures and higher helicopter airspeeds are reached.

The cooling system's total current consumption, while operating at all ambient conditions, is under 10.5 A. This total consists of the TECs at 7 A, the two coolant pumps at 1.5 A each, and the four cooling fans at 0.1 A each. The system's average coolant flow rate is 0.75 GPM. This is about 25% less than what is required for optimal operation of the laser diodes due to higher than expected flow restrictions and pressure drops across the system and to the unavoidable voltage fluctuations present in the helicopter's 28-V power bus that directly affects pump speed and performance. As a result, the average laser power output is about 20% less than what could be achieved at a higher (1.5 GPM) flow rate due to the strong dependence of the diode's output wavelength to the diode's operating temperature. Further improvement in the coolant flow rate, up to 1 GPM, could be achieved by using a gear pump instead of a centrifugal pump. However, there is a trade-off in higher current consumption, weight, and price.

3.1.3 OPO

There are two alternatives for setting up an OPO: external cavity and internal cavity (Figure 4). In the former case, the resonator of the OPO is separate from and is positioned outside of the pump laser cavity. In the latter case, the OPO resonator is embedded inside the pump laser cavity and may have some shared component with it.

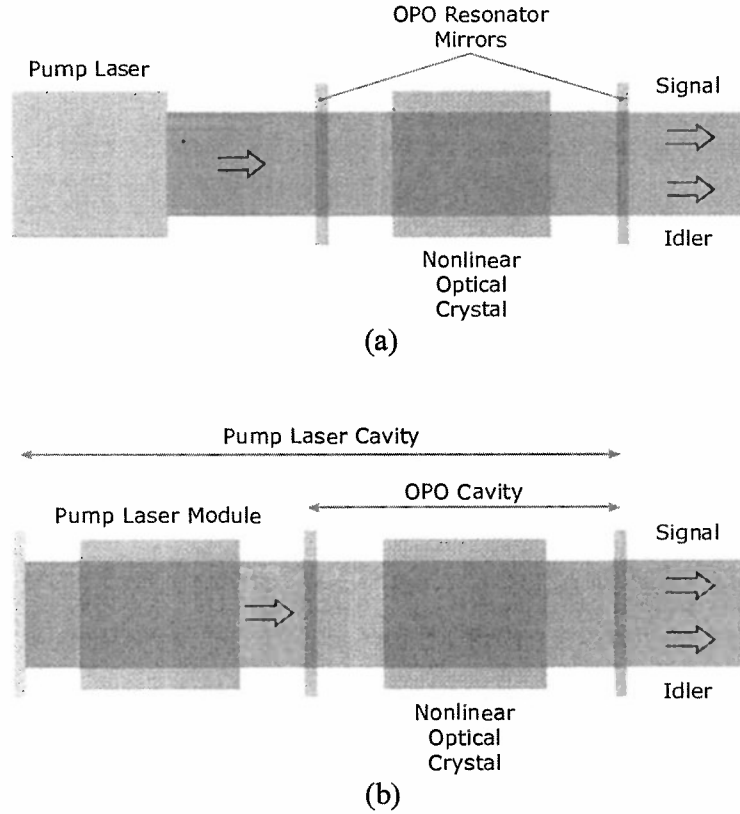


Figure 4. External (a) and internal cavity (b) OPO configurations.

Both configurations can yield high optical conversion efficiencies. However, in our experience, the intra cavity OPO (IOPO) configuration has greater mechanical stability and allows for a more compact laser packaging. For this reason, we chose the IOPO configuration for our laser transmitter design.

One disadvantage of the OPO approach is the relatively low wallplug conversion efficiency of the laser transmitter. We estimate that approximately 0.5% of electrical power supplied to the device is converted into the usable mid-IR output. Maximum energy output obtainable from our OPO is close to 1 mJ per pulse which is limited primarily by optical damage threshold of various OPO components.

3.1.4 Crystal Selection

The choice of a nonlinear crystal is extremely important for the performance of an OPO. Among the nonlinear crystals available for mid-infrared generation, Potassium Titanyl Arsenate (KTA) has a number of properties that make it particularly amenable to moderate-to-high average power OPO. Compared to its popular isomorph, potassium titanyl phosphate (KTP), the arsenate has an extended infrared transmission range out to 5 μm . This property is extremely important for minimizing infrared absorption and thermal effects in a high average power operation. Additionally, KTA exhibits excellent damage resistance to high-intensity pulsed radiation. Relevant optical and nonlinear properties of the KTA crystal are summarized in Table 1.

Table 1. Optical properties of the KTA crystal.

Crystal type	Positive biaxial, point group mm2
Transparency range	0.35—5.3 μm
Damage threshold (10-ns pulses at 1064 nm)	15 J/cm ²
Nonlinear coefficients	$d_{32} = 4.74 \text{ pm/V}$, $d_{31} = 2.76 \text{ pm/V}$
Linear absorption	<0.05%/cm @ 1064 nm, 1533 nm <5%/cm @ 3475 nm
Average refractive index	1.8

The tuning range is determined by the phase-matching properties of the KTA crystal and the specific interaction geometry. Figure 5 shows the tuning curve for a KTA crystal cut for phase matching in the xz principal plane (x -cut). The longest wavelength achievable with this cut under non-critical phase matching conditions ($\theta = 90^\circ$) is 3474 nm. Note that by cutting the crystal for phase matching in the yz plane (y -cut), the long-wave cutoff can be extended to 3647 nm. However the effective nonlinear coefficient for this interaction is lower compared to the xz -plane phase-matching.

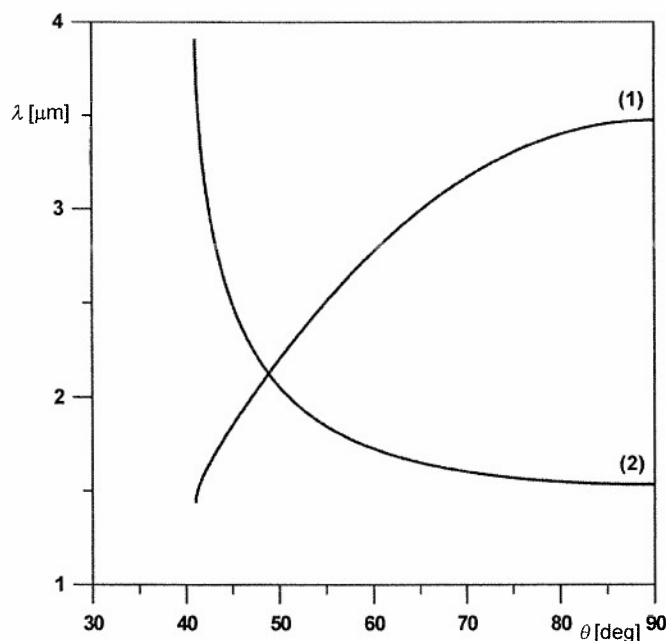


Figure 5. KTA tuning curve. Phase-matching in the xz -plane. (1) idler wave, (2) signal wave. Refractive index data are from reference [8].

The short wavelength cutoff depends of the angle θ of the crystal cut and the maximum amount of crystal rotation in the cavity. The actual crystal rotation angle required to achieve the desirable tuning range is n_p times greater than the internal angle shown in Figure 5, where n_p is the refractive index for the pump wave ($n_p \approx 1.8$). According to data shown in Figure 5, the angular tuning rate can be very high for a crystal cut near 40° . However, operation in this angular range results in a broad spectral linewidth of the OPO, typically on the order of several wavenumbers. Additionally, the nonlinear coefficient is proportional to the cosine of the angle θ and hence is accordingly reduced with a lower cut angle. For these reasons, we choose to operate the OPO with the crystal cut near 75 – 80° , which provides a reasonable compromise between tuning rate, linewidth and efficiency.

3.1.5 OPO Linewidth Considerations

Laser linewidth is an extremely important parameter in laser spectroscopic applications. If the linewidth of the source is too wide relative to the characteristic spectral features of the analyte, the spectrum will not be fully resolved and a smoothing effect will occur. In atmospheric measurement an additional implication of broad linewidth is that absorption contributions from various atmospheric constituents may become inseparable.

To fully resolve methane and water lines in the mid-IR region, the laser source must have linewidth better than $10^{-5} \mu\text{m}$. This narrow linewidth cannot be achieved by an OPO-based source without special line narrowing techniques. Unfortunately, application of line-narrowing

methods results in an extremely complex and sensitive system, which does not lend itself to a compact, military-grade implementation. Consequently, we opted for a free running OPO design that does not employ any line narrowing components. According to our measurements, for the type-II ($o \rightarrow o + e$) parametric interaction in KTA cut near $\theta = 80^\circ$ the resulting linewidth of the OPO source is 1.2 cm^{-1} (Gaussian σ). This parameter is used in simulations of OPO beam propagation through the atmosphere presented later in this report.

3.1.6 OPO Tuning

The frequency agility property discussed above is ultimately related to the OPO tuning method. In this section we briefly review the theory behind the OPO tuning, and then discuss several possible tuning methods. A selection of the angular tuning is made, and specific hardware to implement it is discussed.

3.1.6.1 Review of the OPO Tuning Methods

Frequency agility of a laser-based remote sensor is ultimately related to the tuning rate and tuning range of the laser source. The inherent tuning ability of the optical parametric oscillator (OPO) makes it particularly suitable as the laser source for a multi-spectral remote chemical sensor. However, combining a wide tuning range with a fast rate of tuning in a single device presents a challenging technical problem. A fast, reliable tuning method is essential to the successful implementation of the active multi-spectral remote sensor.

Various methods for frequency tuning the output of an optical parametric oscillator have been established and discussed extensively in literature. The basic problem can be stated mathematically as a set of two simultaneous equations:

$$\begin{aligned} \frac{1}{\lambda_p} &= \frac{1}{\lambda_s} + \frac{1}{\lambda_i}, \\ \frac{n_p}{\lambda_p} &= \frac{n_s}{\lambda_s} + \frac{n_i}{\lambda_i}, \end{aligned} \tag{1}$$

where the subscripts p , s , and i refer to the pump, signal and idler waves, respectively; λ represents the wavelength of light and n represents the refractive index of the nonlinear medium. The first equation reflects the law of energy conservation in parametric interaction, while the second equation expresses the law of momentum conservation. Tuning of the OPO is tantamount to changing the signal and idler wavelengths, λ_s and λ_i . According to equations (1), this can be accomplished through changing the pump wavelength λ_p and/or the refractive indices.

The majority of the tuning methods rely on a certain mechanism for changing the refractive indices for the three optical waves interacting in the nonlinear medium. Such a change of the

refractive indices can be effected through applying an external electric field to the crystal (electro-optical effect), changing the crystal's temperature or changing the direction of propagation and polarization state in an anisotropic¹ nonlinear crystal. The later method is known as the angular tuning and is most frequently accomplished by either mechanically rotating the crystal or changing the angle of the pump beam through the crystal.

In terms of speed, the angular tuning lies between the slow temperature tuning, and the ultra-fast electro-optic tuning. The latter method is characterized by a time constant in the nanosecond range. However, the range of electro-optic tuning is typically limited to a few wavenumbers or less.

Of the non-mechanical angular tuning alternatives, methods based on the use of acousto-optical beam deflectors deserve a special mention. An acousto-optical beam deflector can change the propagation direction of the transmitted beam by modulating it with an ultrasonic acoustic wave inside a specially chosen crystal medium. The beam deviation angle is controlled by changing the frequency of the electrical signal applied to the piezo-electric transducer bonded to the crystal surface. The response time of the device is limited by the time it takes a perturbation to propagate across the aperture of the acousto-optical crystal and is typically in the tens of microseconds range.

An optical parametric oscillator tuned by acousto-optically rotating the pump beam is described by Yang *et al.* [9] The authors used a periodically poled lithium niobate (PPLN) crystal pumped by a 1-kHz Nd:YAG laser. To increase the pump beam angular deviation produced by the AOTF, the authors employed a 3:1 reduction telescope positioned between the AOTF and the OPO. The demonstrated OPO is randomly tunable from 3.2 to 3.7 μm between the shots of the 1-kHz pump laser. An attractive feature of this tuning method is that it involves no moving parts.

Despite its advantages, the above method has a number of significant drawbacks. First, the angular displacement of the pump beam leads to an angular displacement of the OPO output beam. Thus, complex compensation optics must be employed to maintain a coaxial OPO output. Additionally, part of the pump beam energy is inevitably lost due to the inefficiencies of the acousto-optic device, thereby requiring higher power output from the pump laser. Finally, the range of angular beam steering produced by an AOTF does not exceed a few degrees, which is insufficient to cover the required tuning range.

Akagawa *et al.* have taken a different approach to the acousto-optic tuning [10]. Instead of changing the pump beam angle, the authors used an acousto-optic tunable filter (AOTF) to change the frequency of the titanium sapphire (Ti:sapphire) pump laser. The electronically tunable Ti:sapphire laser was used as a pumping source for a KTP OPO. This system can produce maximum idler output of 0.06 mJ tunable from 2.14 to 3.17 μm . Unfortunately, the complexity and size of the complete system make it an unlikely candidate for space constrained applications.

¹ In an anisotropic optical medium, the properties depend on the direction of light propagation.

In another related study, Klein *et al.* demonstrated a PPLN OPO pumped by a tunable ytterbium-doped fiber laser [11]. The system delivers a tunable mid-infrared output with a peak power in excess of 1 W. However, the OPO operates in a continuous wave (cw) mode which is not suitable for range resolved detection. The tunable fiber laser technology is still evolving and at present is not available commercially.

Yet another concept for using an AOTF in OPO tuning was advanced by LaSen, Inc. The idea derives from the well-known principle of building tunable laser sources. First, a laser gain medium with a broad gain bandwidth is selected. Then, certain wavelength selecting elements, such as étalons, gratings, polarization filters, etc. are inserted into the laser cavity to control the spectral output. Although not typically used in this mode, an OPO can be set up to have a broad gain bandwidth. Such conditions occur near the so-called dispersion phase-matching point, where the OPO gain bandwidth can be several hundreds of wavenumbers, as opposed to just a few wavenumbers under normal conditions. By combining the wide gain OPO with an electronically tunable spectral filter such as an AOTF, it is possible to construct an all-solid-state OPO/tuner.

The layout of the OPO/tuner module is shown in Figure 6. The output coupler, beamsplitter and HR-mirror form resonator for the signal wave. An AOTF inserted into the OPO resonator provides the wavelength selection and line narrowing.

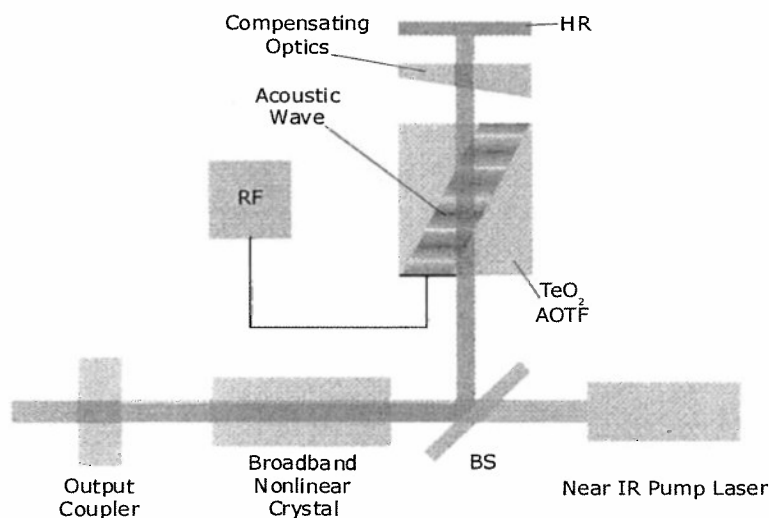


Figure 6. LaSen's mid-infrared OPO/tuner design based on an intracavity AOTF.

Despite its considerable potential, this configuration was not chosen as the prototype for the implementation under the Phase II SBIR project. Two specific areas raise concerns. First, attenuation of the signal wave by the AOTF will result in an increase of the OPO threshold. Thus, a higher energy pump source is required to pump the OPO thereby making the device more susceptible to optical damage problems. Second, the dispersion phase matching point in a

KTA crystal occurs near the idler wavelength of $4.2\ \mu\text{m}$ which is close to the edge of the crystal transmission region. Although these technical challenges can be potentially overcome, in the interest of expediting the progress towards a fieldable system, it was deemed necessary to look for a less risky technical approach.

3.1.6.2 Angular Tuning of the OPO

Mechanical crystal rotation is by far the most frequently used method of OPO angular tuning. The tuning range, speed and accuracy achievable with this method depend on the specific type of the actuator used to rotate the crystal. As an example, consider the tuning mechanism used in LaSen's Lidar II system (Figure 7). Wide-range angle positioning is accomplished via a precision rotation stage (National Aperture MM-3M-R model) driven by a brush-type DC motor. The rotation stage is equipped with a position encoder, which provides the feedback signal for the servo control loop. This method of tuning allows for excellent precision and repeatability, albeit at a slow rate. The fast switching between the on-line and off-line required for the DIAL method is accomplished by LaSen's proprietary piezo-driven angle shifter. The piezo-tuner can change the crystal's angular position by up to $5\ \text{mRad}$ in less than $10\ \text{ms}$. This angular shift is equivalent to the wavelength shift of about $5\ \text{cm}^{-1}$ which gives a sufficient spectral separation between the on-line and off-line pulses in a typical methane measurement. Unfortunately, with the piezo-actuator design it is not possible to increase the tuning range by much without sacrificing speed.

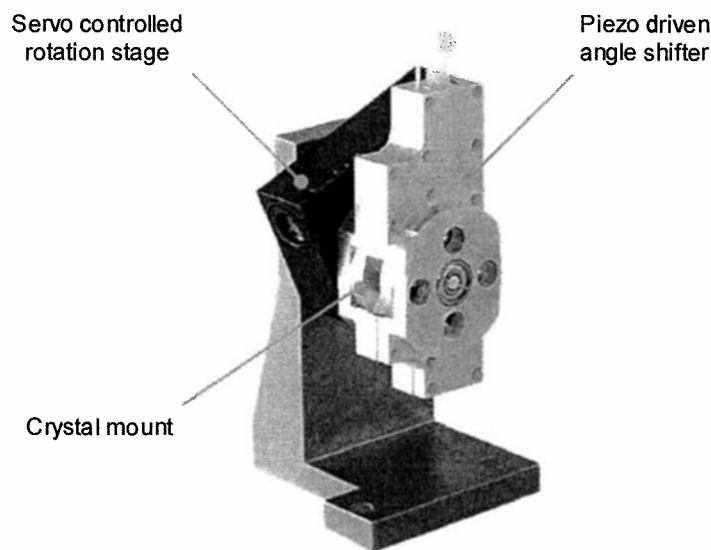


Figure 7. Opto-mechanical angular tuner used in LaSen's Lidar II system.

It is highly desirable to develop a tuning mechanism that would combine the wide range of tuning achievable with rotation stages with the speed of piezo-actuator technology. These properties are indeed found in galvanometric scanners. Such scanners are widely used for beam

steering applications requiring high speed and accuracy. A typical scanner has a mirror mounted to the rotor shaft. For the OPO tuning application, the mirror would be replaced with a crystal in an appropriately designed mount (see Figure 8). A scanner also includes a certain type of position sensor that provided a feedback signal for the servo loop control.

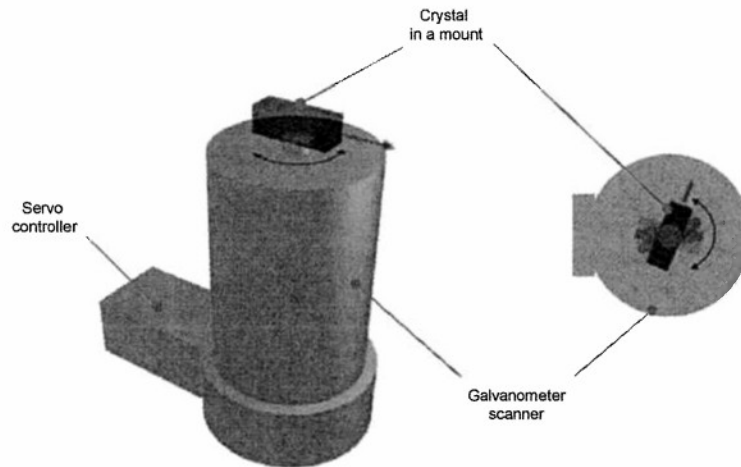


Figure 8. A high speed OPO angular tuner using a galvanometric scanner.

3.1.6.3 Crystal Mount Design and Moment of Inertia

Before addressing the selection of a galvanometer for OPO tuner implementation, we must consider the mechanical characteristics of the expected load. The ability of a galvanometer to swing a load such as a mounted crystal is ultimately dependent on the inertial characteristics of the load. The best performance of a galvanometer system typically exists when the moment of inertia of the load is approximately the same as the rotor inertia, specified as a balanced load. Torque is being wasted on the rotor if a small load is placed on a large rotor. Conversely, a small rotor cannot deliver enough torque to drive a large load. Besides, matching the inertia of load, the mounting structure should be mass balanced with low inertia with respect to the moving axis and relatively rigid and stiff to properly support the optics. Thus, it is necessary to calculate the combined moment of inertia of a KTA crystal with a suitable mounting structure.

For calculating the moments of inertia, two sizes of KTA crystals were considered. Table 2 shows the combined moments of inertia of the crystal and mount assembly for different choices of material for the mount.

Table 2. Calculated moment of inertia of KTA and mount assembly

Materials of Interest	Moments of inertia of the crystal mountings (gm-cm ²)	
	5 x 5 x 15-mm KTA	6 x 6 x 15-mm KTA
Magnesium	0.489	0.667
Beryllium	0.503	0.683
Aluminum 7075-T6	0.615	0.818
Titanium	0.823	1.069
S. Steel	1.221	1.546

Mechanical design of a rigid crystal mount possessing a low moment of inertia is shown in Figure 9.

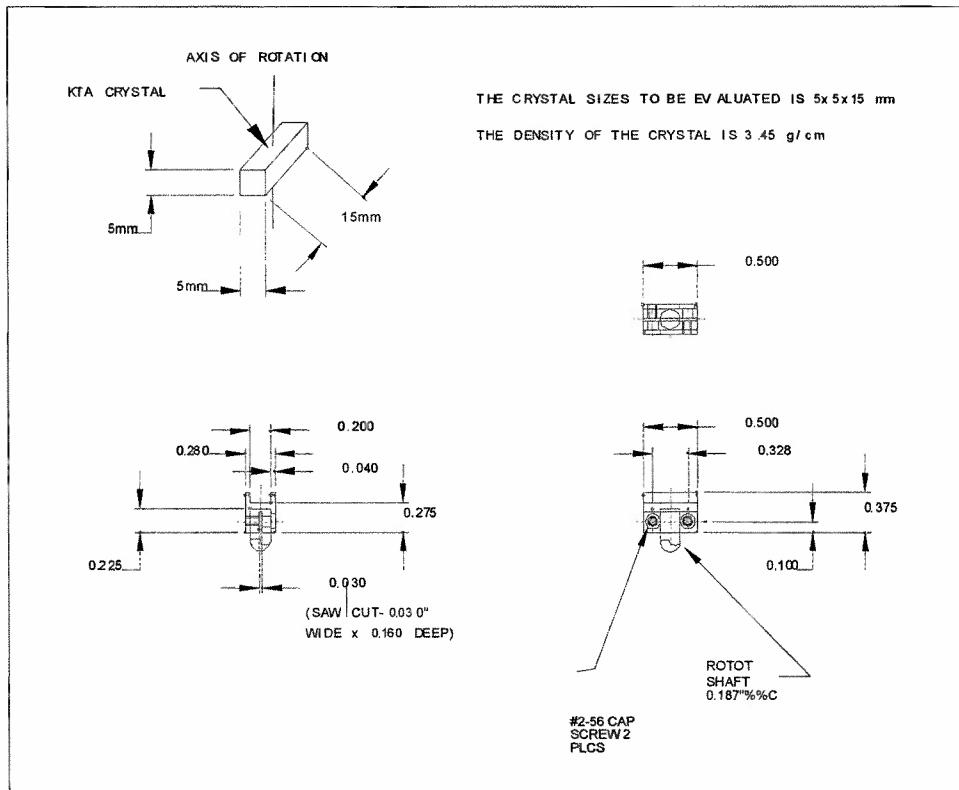


Figure 9. Mechanical design of the KTA crystal mount.

3.1.6.4 Galvanometric Tuner Characteristics

Based on the moments of inertia of the crystal mounting assemblies, we selected the galvanometer scanner model LBS-6124 manufactured by Lasesys Corp. (Santa Rosa, CA) This device has rotor inertia of 1.0 gm-cm^2 , and maximum scan angle of $\pm 10^\circ$ (mechanical). The company also provided the servo control board SCA-754 for the selected galvanometer model. Based on the specified load requirements, the manufacturer performed laboratory tests to calibrate the performance of the selected galvanometer. The first parameter assessed in the tests was the motion capability with step-and-settle tuning.

The step-and-settle tuning application is used when the KTA crystal is rotated rapidly from one position to another and the optical system is being utilized only at the ends of motion. The purpose of the test was to determine for each crystal size the highest step rate capability to move the crystal through small angles and to settle to within specified error bands. The operational conditions considered were every combination of step sizes of 0.75, 1.5, and 3 degrees, and settling to within ± 0.003 , ± 0.01 , and ± 0.03 degrees of the final positions.

The selected galvanometer system was operated in the closed-loop configurations with the built-in position feedback sensors and servo controllers. Closed-loop servo controlled galvanometers maintain absolute positions by using feedback signals from the position sensors to dampen the natural oscillations of the galvanometers. When a galvanometer is being commended to a constant position in a step-and-settle tuning mode, the deflector will be still moving slightly in the axis of rotation, due to noise existing in the position sensor and servo control electronics. A step response is completed when the scanner enters the command position and stays within the setting tolerance, centered on the final position. The step time, or the step plus settling time, is commonly measured from the initial starting of the command waveform to the first instance when the settling tolerance is achieved.

The manufacturer performed several laboratory tests to calibrate the step times of the LBS-6124. The load used during the calibration is a steel chunk with inertia of 0.923 gm-cm^2 . The tests were conducted by driving the galvanometer with command waveforms of single amplitude and frequency and the results are listed in Table 3.

Table 3. Step-and-settle tuning response for the LBS-6124 galvanometer.

Step Angeles (Deg.)	Step Time (μsec)	Accuracy (Deg.)
0.75	688	± 0.005
1.50	784	± 0.015
3.00	952	± 0.030

Since the KTA crystal tuning is applied for its transmission application, the step angles used for conducting the step tuning tests are the mechanical peak-to-peak angles of excursion. The step

response time is defined as the transitional time of the galvanometer's response from 10% to 90% of its peak value. The step time is measured from the initial arrival of the command signal to the first instance when the galvanometer enters and stays within 1% of the final commanded position. The 1% settling tolerance is widely used by the scanner manufacture to measure the step time of their scanners. According the test results, there is a difference, approximate 200 μ sec, measured from the initial arrival of the command waveform to the initial motional response of the galvanometer. The lag time is caused by the inductance of the coils built inside the motor assembly and it stays at a fixed amount for a given scanner.

The second parameter assesses in the manufacturer's test was the motion capability with sinusoidal tuning. In this mode, the crystal and its mount are rotated in a sinusoidal motion with a fixed angular range in a repetitive manner. The main purpose of this test is to determine the maximum frequency of the motion that can be feasibly achieved for each given vibration amplitude. The vibration amplitudes of interest are ± 5 , ± 10 , ± 15 , ± 20 and ± 25 mechanical degrees.

The galvanometer and loading inertia used for conducting this test are the same ones as used for the step tuning tests. Due to the limitation of the angular excursion on the selected galvanometer, only one test could be performed for the vibration amplitude of ± 5 degrees. The maximum frequency of motion is listed in Table 4.

Table 4. The maximum frequency of motion for LBS-6124 galvanometer.

Vibration Amplitudes (Deg)	Maximum Frequencies of Motion (Hz)
5	300
10	N/A
15	N/A
20	N/A
25	N/A

The time of response is dominated by the torque to inertia ratio. When a scanning system is running in a continuous sinusoidal motion, the resonance of the scanner with load and constrains of thermal dissipation will additionally limit the scanner's efficiency and bandwidth. Due to the weight of the position sensor attached to the rotor, a galvanometer with a built-in position sensor has a higher combined inertia than the one without a position sensor. Questions concerning whether much faster sinusoidal motions can be obtained by running scanners that do not contain a built-in position sensor were addressed to the manufacturer. Theoretically, open-loop scanners without built-in position feedback sensor have higher torque to inertia ratios compared with the closed-loop ones. However, open-loop galvanometers are running without position feedback, which means the absolute positioning accuracy is relying on equalizing forces between the magnet torque applied to the rotor and the attached torsion bar. So practically, open-loop galvanometers are typically less accurate and slower than their closed-loop counterparts. Normally, the maximum bandwidth of an open-loop galvanometer is rated up to 80% of its

resonant frequency, while a closed-loop counterpart is rated up to 100%. Closed-loop servo controllers take into account the instantaneous position when calculating the appropriate motor drive current to eliminate severe overshoots. When a closed-loop galvanometer is combined with a closed-loop servo controller, the system can be optimized to achieve the desired dynamic response with highest accuracy and speed.

An important consideration pertains to the expected lifetime of a galvanometer-based OPO tuner. Galvanometers are designed to be operated with random moves over the full scanning field. Commanding repetitive small angle motions of any ball bearing scanners will likely lower the usable lifetime because bearing lubrication is not adequately distributed which causes uneven wears on bearings. Since ball bearing are the only component exposed to mechanical wear in a moving magnet galvanometer, the cycle life of bearings, when used in a limited small angle rotation, is de-rated by a factor of 5 to 10 when compared to that same bearing used in a scanner rotating 360 degrees.

3.1.6.5 Accuracy and Adequacy of Position Feedback Signal

The absolute position accuracy of a closed-loop scanning system is affected by many factors such as dither, jitter, wobble, thermal drifts, repeatability, and linearity of position sensor. When a scanner is being commanded to a constant position, such as at the beginning or end of a step scanning, the deflector will be moving slightly in the axis of rotation, due to noise existing in the scanning system. This noise motion is referred to as dither. Some of the noise comes from the scanner's position detector electronics; however a large portion of this noise results from the servo controller electronics. Typically, dither values range between 3 and 25 μRad depending on the scanner/servo combination.

Jitter is dither plus additional mechanical noise or rumble created by the ball bearings in motion. Jitter is considered when observing sinusoidal scanning applications, where as dither is more applicable to step scanning applications.

Wobble is motion perpendicular to the axis of scanning motion and is caused mainly by moving unbalanced loads. Wobble can also caused by imperfect bearing geometry and long-term wear. A balanced rotor assembly with load is necessary for minimizing wobble that produces across-scan errors. Most new style bearing scanners incorporate a bearing 'preload' to maintain a consistent point of contact between the bearings and rotor assemblies. If unbalanced loads or resonance of the load do not surpass the preload force, the wobble typically stays below 5 μRad .

The thermal drift includes offset drift and gain drift. Offset drift is the change with temperature of the position detector's zero position. The gain drift is the change with temperature of the scanning angle. The position feedback electronics compensates for some level of temperature drifts. To reduce scanner drift induced by temperature changes, most scanners are available with a temperature sensor for thermal regulation by an external controller. This helps maintaining a consistent temperature within the position detector electronics to minimize the scanner offset and gain drift. Such regulation can reduce thermal drifts by an order of magnitude or more. In most

step-and-settle scanning, power dissipation in the scanner is minimal, and therefore the scanner requires little heat sinking. Contrarily, in fast sinusoidal or high-duty-cycle step scanning, significant heat can be generated in the motor, and sufficient heat-sinking is critical. Optimum heat sinking is desired to maximize the scan frequency and prevent damages to the scanner caused by overheating. Typically, the scanner mount is designed to attain sufficient heat dissipation. To maximize heat flow from the motor case to the heat sink, the surface area of the mount should contact as much of the scanner as possible. Surface finishing should not exceed 0.8 μm , otherwise thermal grease between the two surfaces should be used.

When a scanner is commanded to return to the same position as part of a series of steps, the consistency with which the scanner returns to this position is referred to as repeatability. This parameter is more a characteristic of the scanner's position detector than the servo controller. Also, repeatability will be gradually degraded due to uneven bearing wear occurring in a repetitive small-angle scanning. Repeatability of a galvanometer is specified by the manufactures as a result of a closed-loop performance with a balanced load. In other words, the repeatability cannot be measured without position feedback sensors and servo controllers. Typical short-term repeatability values are around 5 μRad . Long-term repeatability requires considerations on mechanical wear and thermal drift.

Linearity of position sensors are measured as the ratios of position readouts of the rotor shaft to the output signals of the position sensor. Linearity is also commonly specified as a parameter for a galvanometer operated in closed-loop applications.

The LBS-6124 galvanometer is equipped with an electro-optical position feedback sensor. A laser diode (LD) light source is embodied in the scanner's body and the reflected LD beam is scanned across a Silicon linear detector. The polarity and ratio of the difference and sum of the electrical currents from each segment of the detector determine the angular position of the deflector. The position sensor currently installed in the LBS-6124 is a 16-bit detector with 15-bit repeatability. The 15-bit repeatability is specified to cover the 20 degree mechanical peak-to-peak angular range. The position sensor itself has a pixel resolution of 3 μm which has an equivalence of 10 μRad . According to the statements made by Lasesys, the proximity of the built-in components plus their smaller mass has the advantage of producing a compact, rigid design with a reduced inertia load for galvanometers. This technique is also stated less sensitive to temperature changes than those capacitive position sensors currently used by other manufactures. Lasesys is holding a patent on the design of applying the electro-optical position sensor to galvanometric and resonant scanners. Since the company claims that adding the servo controller should not causing degradation on the repeatability, or the resolution, in closed-loop systems. The short-term repeatability, also specified as the short-term absolute accuracy, of the LBS-6124 is specified at 10 μRad which is equivalent to the resolution of the position sensor.

3.2 Receiver Design

We opted for a very simple receiver design employing a single element refractive optic (lens) positioned in front of a cryo-cooled infrared photodetector mounted in a standard LN_2 dewar (Figure 10). In this design, the receiver's field of view is determined by the ratio of the detector

size to the focal length of the lens. The size (diameter) of the lens determines the receiver's light collecting ability. This design is especially convenient when a wide field of view and a relatively small collecting aperture (less than 2" diameter) are required. Since the receiver measures the total amount of backscattered energy ("energy in the bucket"), imaging performance of the receiver optics is irrelevant. We have successfully used both Ge lenses and plastic Fresnel lenses as primary elements in this receiver.

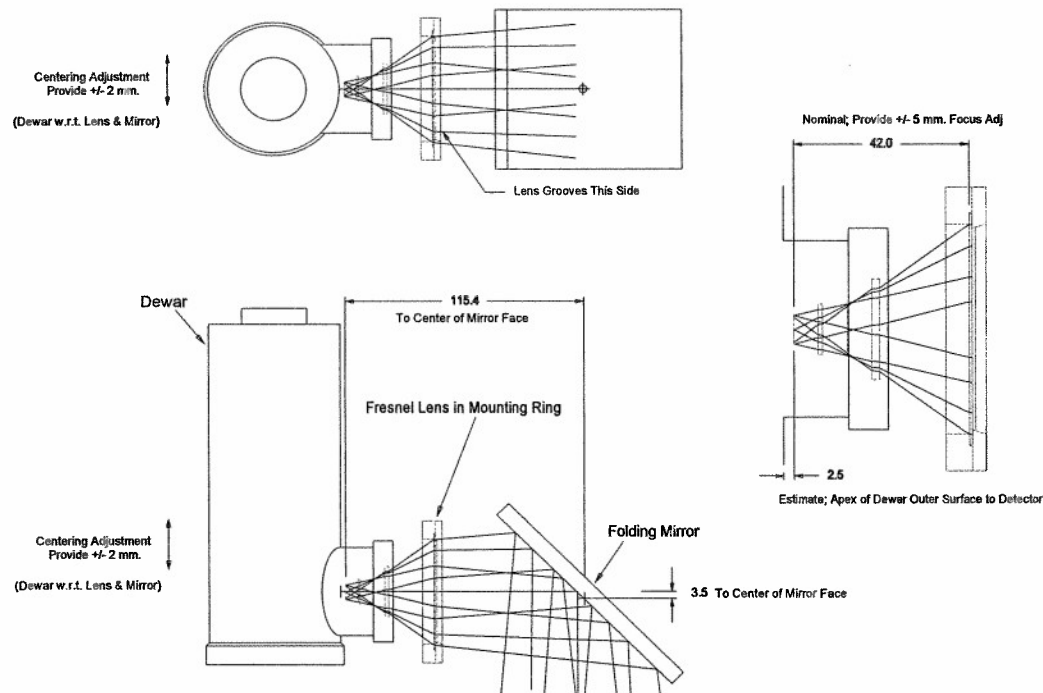


Figure 10. Receiver optical layout.

3.3 Overall System Layout and Parameters

In developing the breadboard prototype of the compact airborne lidar system, we opted for a simple planar design concept. All of the system components are rigidly mounted to a single 0.5" thick aluminum base plate with footprint dimensions of 36" \times 22". Although this design introduces a heavy weight penalty (the baseplate alone adds 35 lbs to the overall system weight), it is by far the most forgiving design for system prototyping since the relocation and adjusting of components can be easily accommodated.

The general system layout is shown in Figure 11. The mid-infrared laser beam is turned 90° twice in the plane of the baseplate by mirrors M1 and M2. It is then turned toward nadir by the transmitter mirror M3. Receiver mirror M4 turns the reflected beam onto the receiver's optical axis. Since the transmitter and receiver turning mirrors are fixed in the prototype, the pointing and aiming of the laser beam is accomplished by steering the entire sensor package.

The baseplate has four openings: for the transmitted beam, received beam, the rangefinder, and the digital camera. A motorized shutter mounted to the bottom surface of the baseplate seals the openings during takeoffs and landings.

Beamsplitters BS1 and BS2 deflect a portion of the outgoing beam towards energy detectors D1 and D2 for energy monitoring and spectral calibration purposes, respectively. A gas absorption cell (AC) is placed in front of D2 and contains a known concentration of the calibration gas.

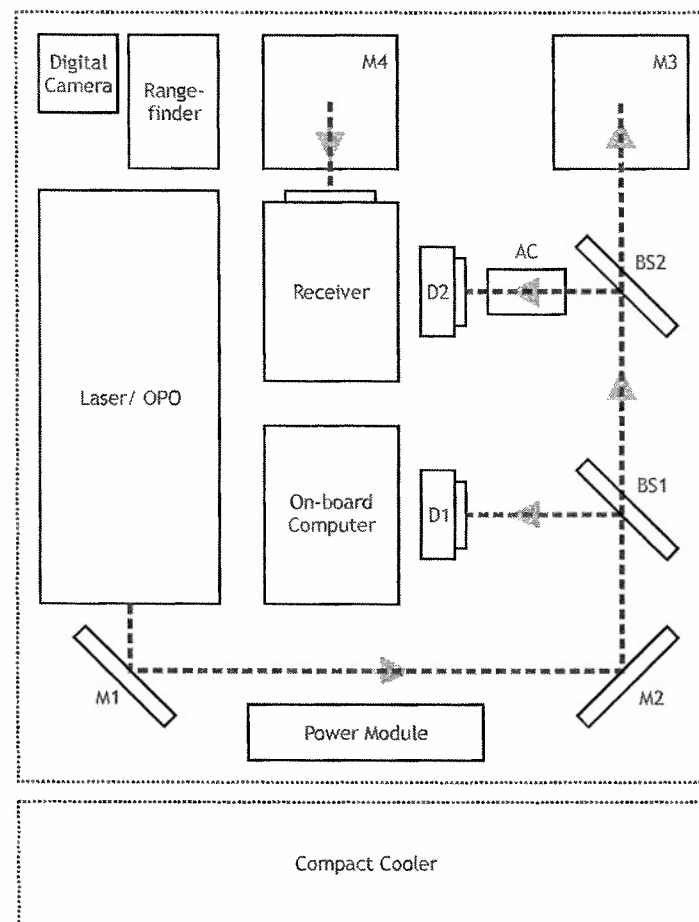


Figure 11. Overall system layout.

All optical components are rigidly mounted to the baseplate to ensure that the optical alignment is maintained under all expected vibration loads. Additionally, the baseplate itself is vibration isolated from the aircraft mounting system. This approach has guaranteed the system's long-term mechanical stability even when operated on a high vibration rotary-winged platform.

The compact cooler is assembled on a separate sub-plate and mounted behind the main sensor package. The main reasons for separating the cooler and sensor packages are to minimize any

induced vibration and thermal load from the cooler components into the sensor package. Additionally, having a separate cooler package allows for easier modifications and upgrades of the cooler system, or installation of newer more efficient coolers in the future. This may allow for the development of higher repetition rate laser systems.

The power for the lidar system is supplied by the aircraft's 28 VDC bus through an umbilical cable. The onboard power module transforms, conditions and redistributes the aircraft power to sub-systems and components. When the laser is operating at a pulse repetition frequency (PRF) of 400 Hz and the cooler is at maximum load, the entire lidar package draws 25 A at 28 VDC from the aircraft.

The rangefinder is a ruggedized version of a commercially available laser rangefinder. It fires approximately 240 times a second to accurately determine the altitude of the lidar system above the ground. The altitude reading is used in the analysis of chemical concentration data.

The on-board computer, or control module, is a set of CPU and data acquisition (DAQ) boards used to receive and implement commands from the operator's control laptop computer, to control the system timing, to receive and pre-process all incoming data from various on-board detectors and sensors, and to transmit the data stream back to the operator's control laptop computer. It is connected to the control laptop through Ethernet connection included in the umbilical cable.

A commercially available GPS system is mounted inside the aircraft and is used to accurately and continuously log the system's position. The GPS unit has an update rate of 5 Hz and is WAAS enabled, allowing positional accuracy of less than 10 feet. It sends coordinates directly to the operator's control laptop so that this data can be incorporated into the lidar's data stream. In the event a chemical release is detected, its exact location can be determined.

A small digital video camera bore sighted with the laser transmitter is used to record the visual images of the target area. The camera records one image every second and has 40-deg field of view which ensures a complete overlap of ground images. The imaging data is crossed referenced with GPS and chemical data, providing an auxiliary tool to target identification.

The overall weight of the prototype lidar package (without aircraft mount and control laptop) is 250 lbs. Its overall dimensions are 49" x 30" x 13".

3.4 Onboard System Controller

The onboard system controller module performs multiple key functions in the lidar system. It receives, processes, and implements all commands given to it from the operator's control laptop computer. It controls the timing and firing of the laser system. It receives / acquires all signal data from various sensors. It pre-processes and integrates the signal data into a usable data stream. It then sends all data back to the operator's control laptop computer.

Many factors were considered in determining the specifications for the on-board controller unit. The two primary factors were: 1) the expandability of the system (clear roadmap for future

development), and 2) the ability to seamlessly integrate the unit with the lidar's various sub-systems. Other factors, such as unit weight and power consumption were considered secondary. In addition, it was decided that the entire control module (including its connectors and shock mounts) would have to fit within the confines of a 7.5" × 7.5" × 11" volume, which posed a number of technical challenges.

The specifications for the central processor unit (CPU) could be roughly estimated based on the performance of the previously used PC104 based control modules, which could barely handle a maximum data rate of 200 pulses per second when using a 300-MHz CPU. Taking into consideration the planned future upgrade of the system to a data handling capacity of 1000 Hz, it was determined that a CPU with a speed of approximately 1.5 GHz was required. Unfortunately, these types of CPUs fall into a higher class of processors that tend to be very power hungry (consuming approximately 200 W), are much larger in size, and typically require some form of active cooling. Recently however, the Intel Corporation unveiled a new series of low-power processors designed for embedded applications, the Core Duo (released in 2006), and the Core Quad (scheduled to be released in 2007). These processors, when operating at a CPU speed of 1.6-2.1 GHz, offer a much lower thermal load of 30-50 W. Unfortunately, these new processors have not yet become widely available. It was therefore decided that a different processor would have to be used. After many comparisons, it was determined that an Intel Pentium M CPU would be adequately suited for the lidar's communication, command, control, and data functions. Additionally, this processor has a clear development roadmap for future system upgrades to Intel's Core series of processors.

We decided that Microsoft's Windows XP (WnXP) Embedded would be the best choice for the control module's software operating system (OS) due to its availability and support. Unfortunately, WnXP does not offer a real-time capability. Its latency period is typically on the order of 10—15 ms. Therefore we decided that all real-time processes could be outsourced directly into the FPGA/ASIC hardware of the digital acquisition (DAQ) cards themselves, leaving the sorting and pre-processing of the incoming data to the WnXP OS. An additional benefit to using Windows XP is the large number of software drivers and development tools that are available for it. In addition, the general familiarity with the OS, due to its general widespread use in other applications, greatly reduces software and system development time and costs.

When selecting a CPU board type or format, the following system standards were reviewed: cPCI (compact-PCI), ePCI (PICMG 1.0 or 'PCI-blade'), and the PC104. Special attention was given to the availability of DAQ cards, overall system dimensions and price for each standard. A summary table of the comparison of various characteristics for each type of system is shown below in Table 5.

Compact-PCI (cPCI) systems occupy the high end of the spectrum, while PC104 and ePCI boards fill the medium and economy niches. Compact-PCI systems are typically 2-3 times more expensive than ePCI systems due to specific market requirements (mostly military) and small production quantities. They are, however, much more rugged than their ePCI counterparts. Additionally, most manufacturers typically offer the newest innovations and features (i.e. faster CPU speeds or better DAQ cards) on their cPCI product lines first. They are also available in standardized modules for quick assembly. The drawbacks to the cPCI systems are their

backplanes and chassis dimensions. Even the smallest systems (having at least two cPCI open slots) are too large and are unable to fit in the existing available space in the lidar. Additionally, their excellent chassis ruggedness comes at the added expense of 15-20 lbs of weight and \$5-8k in costs. As a result, the minimum hardware cost for an assembled cPCI DAQ system would be in the \$12-15k range. Despite these size, weight, and cost limitations, the cPCI platform standard remains an excellent choice and will be considered for possible future upgrades and developments in the compact airborne lidar system.

PC104 systems are the most compact and lightest of the three platform standards. They tend to be very rugged and are moderately priced. They have features that fall in between the high-end cPCI and low-end ePCI systems. However, they have several drawbacks. While some manufacturers of PC104 systems offer ready-to-use chassis, the variety of models available are limited. Additionally, their dimensions and connector arrangements usually do not match the existing restrictions inside the lidar. Also, the availability of software, DAQ cards, and parts is very limited. The ability to upgrade the system is also very limited.

PCI-blade (ePCI) platforms on the other hand are the most widely used system in commercial applications. As a result, they typically have low prices, wide availability, and large number of accessories and software available. Their half-size board versions (shorter than 8") are very light and compact and are required in the tight space restrictions of the lidar. Due to the availability of components and software, their development time is very short and they have excellent upgrade potential. This helps reduce overall system development costs. Unfortunately, there are few, if any, standard chassis available for the ePCI. As a result, the chassis has to be custom-designed for each particular board. They also tend to be less rugged than their cPCI and PC104 counterparts. Even with these limitations, they make for an excellent overall choice.

Table 5. Comparison of various system standards.

	cPCI (industrial)	PC104 (milspec)	ePCI (commercial)
System price	Very high	Medium	Low
Parts availability	Good	Poor	Good
COTS chassis	Standard	Limited	N/A
Weight	Heavy	Lowest	Low
Dimensions	Bulky	Most compact	Compact
Ruggedness	Good	Excellent	Poor
Software & Drivers	Excellent	Poor	Excellent
Upgradeability	Good	Poor	Excellent
Development time	Excellent	Poor	Excellent

Based on an analysis of the above comparisons, it was determined that a half-sized Pentium-M ePCI board would provide the best solution for a quick and inexpensive development and prototyping application with a clear path for future upgrades.

The system control module's specifications were set as follows:

Computer:

CPU type: Intel Pentium M

CPU speed: 1.6-1.8 GHz

CPU board: ePCI (PICMG 1.0) half-size format

Backplane: at least 3 PCI slots available

Operating System: Microsoft Windows XP Embedded, hardened environment

Dimensions: not to exceed 7.5" × 7.5" × 11" (including all connections and mounts)

Net weight: less than 6 lbs

Power supply: wide input voltage range of 8-36 V, automotive grade

Power consumption: less than 50 W (or less than 2 A at 28 V)

DAQ boards:

DAQ acquisition channels: 3 (upgradeable to 4)

DAQ speed: up to 1.25 MHz per channel

DAQ resolution: 12 Bit (upgradeable to 16 Bit)

DAQ synchronization: internal, real-time

Pulse repetition frequency: up to 1000 Hz (with CPU load under 50%)

A simplified block diagram of the on-board controller network is presented in Figure 12.

The central processor unit (CPU) and data acquisition (DAQ) cards communicate through a PCI bus. The onboard computer can communicate with operator's console laptop by means of high-speed (100Mb) Ethernet line using TCP-IP protocol. Data acquisition cards digitize real-time data from several photodetectors and store it into onboard memory through two DMA channels. The DAQ cards also provide synchronous TTL trigger waveforms for the current driver, galvanometer scanner controller, and a Q-switch driver, all of which provide timing signals for the laser/OPO unit. Additionally, several RS232 serial communication lines are used for communication with galvanometer controller and the rangefinder.

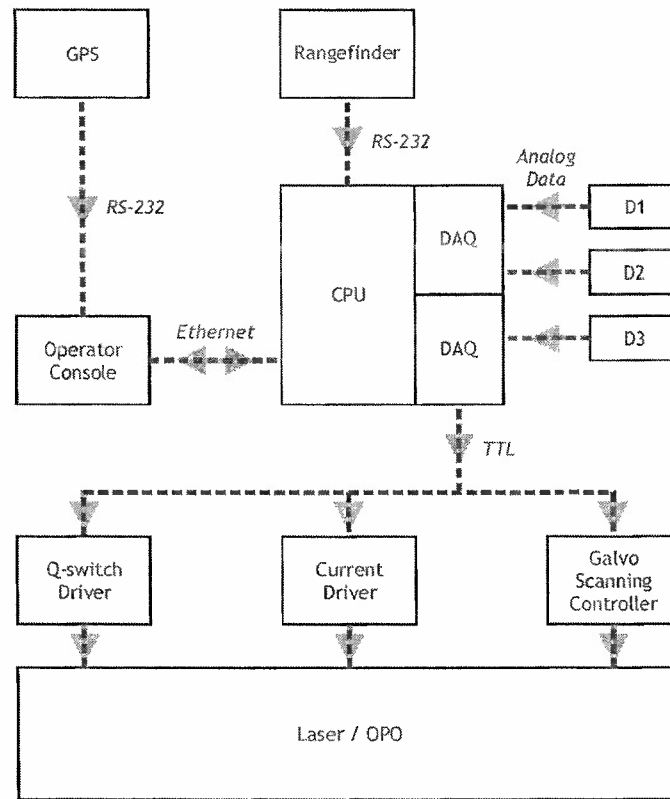


Figure 12. Onboard controller architecture.

To ensure uninterrupted collection of data, all real-time functions are outsourced to the two DAQ cards, whose time clocks are internally synchronized through a RTSI bridge. Prior to the start of data acquisition, the memory buffers of DAQ cards are populated with appropriate trigger waveforms and both analog strobe and digital trigger outputs are enabled simultaneously. The internal ASIC fabric provides real-time performance, not affected by the Windows XP latencies. This trick makes it possible to overcome the repetition rate bottleneck which typically limits the pulse repetition rate to about 100 Hz due to the 10-ms reset time of the DAQ cards before each pulse.

The system timing diagram of TTL trigger pulses is presented in Figure 13. The four trigger pulse sequences shown in the diagram control: a) the analog input gate of the DAQ cards, b) galvanometer controller advance, c) laser diode current gate, and d) Q-switch gate. The relative delays of timing signals (a-d) are appropriately adjusted with respect to the leading edge of the master trigger pulse to provide optimal conditions for laser generation, galvanometer movement and signal acquisition. The master trigger pulse is internally generated inside DAQ cards and is not available as an output, simply providing a convenient 'zero' offset for the rest of the delay triggers.

After acquisition of each signal waveform is complete, raw sensor data is transferred to the physical memory of the main board through DMA channels and subsequently processed at the

CPU of the onboard computer in a non-real time manner. It is then transmitted through the network to the operator's laptop for storage.

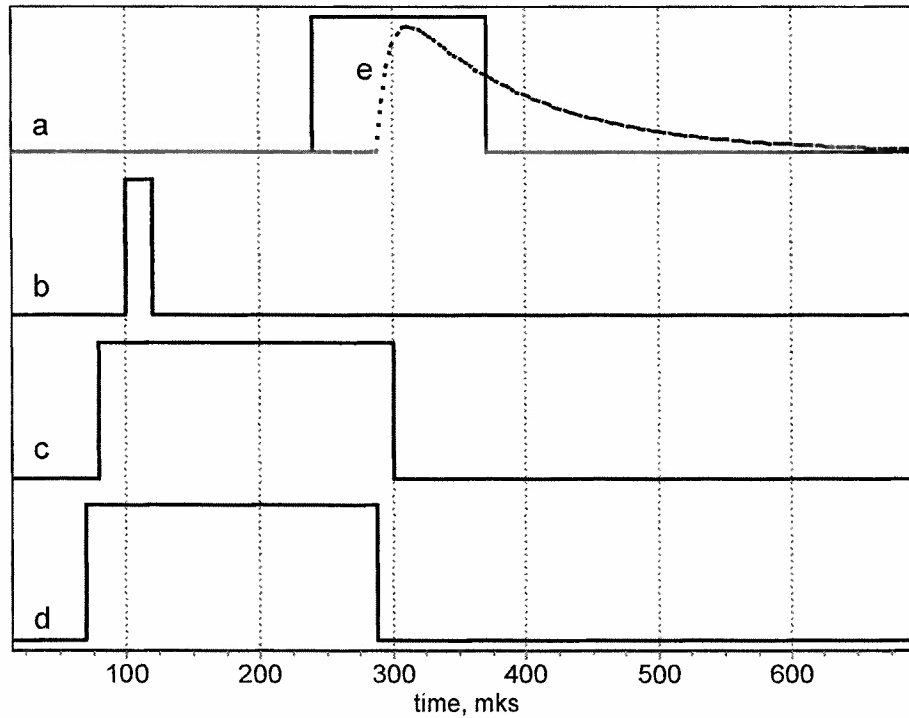


Figure 13. Lidar controller timing diagram. (a) analog input gate of the DAQ cards, (b) galvanometer advance, (c) laser diode current gate, and (d) Q-switch gate. Curve (e) shows a typical signal waveform.

3.5 Real-Time Communication and Data Reporting

As a sensor intended for future deployment on unmanned aerial vehicles (UAVs), the mid-IR airborne lidar must support a remote mode of operation. In this mode, the sensor will exchange commands and data in real time with a ground-based command center via a suitable communication channel. The remote capability will allow for a seamless integration of the sensor into the Future Combat Systems (FCS) network. Although hardware implementation of the remote operation mode is not a part of the current effort, communication and data reporting requirements must be analyzed and available solutions need to be identified. We started the analysis with investigation of the bandwidth requirements for the communication channel.

3.5.1 Data Types. Bandwidth Requirements Analysis

As most remote sensors, the mid-IR lidar has an asymmetric data exchange between the operator and the sensor in the sense that a higher bandwidth is required in the direction sensor to operator while only a relatively small amount of data has to be transmitted from the operator to the sensor. Information from the lidar consists of chemical data, GPS coordinates and video/imaging data. Meanwhile only compact control commands and mission parameters have to be sent to the sensor (Figure 14).

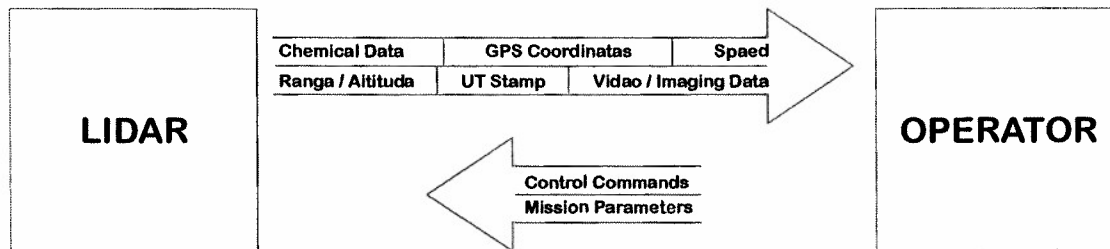


Figure 14. Data exchange overview.

A common solution for a system with asymmetric communications is for the transmitter to have a higher bandwidth than the receiver. However, restrictions imposed by weight and size limitations of the airborne platform require a different approach. Data throughput requirements of the sensor and bandwidth capabilities of common Commercial Off-The-Shelf (COTS) communication systems (as well as military communication channels) need to be compared, and data reduction and/or compression algorithms must be implemented if necessary.

To reduce the communication channel bandwidth requirements, most of the processing and analysis of raw sensor data will be performed by the on-board system controller. Processed data will be assembled into compact packages and transmitted to the command center through the communication channel. Each package will contain chemical concentration data, auxiliary sensor data, and system status information (health monitoring). The chemical data will comprise an array of real type numbers representing measured concentrations for the chemical species of interest. We currently estimate the maximum number of simultaneously monitored chemicals to be 20. Additionally, statistical indicators of the quality of the concentration estimates must be sent along with the corresponding data. For the purposes of the present analysis we assume that the statistical overhead will be 2 real-type numbers for every concentration estimate. Aside from the chemical information, each data package will also contain range, Global Positioning System (GPS) coordinates, speed, and Universal Time (UT) stamp (see Table 6).

Table 6. Lidar data package.

	Number of Elements	Data Size (Bytes)	Data Type
Chemical	20	6 X 20	Float
Statistical	20 x 2	6 X 40	Float
Range	1	6	Float
GPS coordinates	2	2 X 12	ASCII
Speed	1	6	Float
UT Stamp	1	12	ASCII
Health monitoring	10	10 X 6	Float

Assuming that the data shown in Table 1 will be updated once every second, a low bandwidth communication channel should be sufficient since the required maximum connection speed will be less than 1 Kilobit/Sec (Kbs)

Streaming video, on the other hand, requires a significantly higher communication bandwidth. Table 7 compares different compression algorithms and their associated bandwidth requirements. Even with the best compression and lowest resolution (only 352×288) it is necessary to have a 64-Kbs channel to transmit streaming video. Along with the high bandwidth requirement, streaming video has other disadvantages such as low image resolution (under 1 megapixel). Furthermore, it is difficult and inefficient to search and index video stream. Additionally, video information is essential for dynamically changing situations that need to be tracked in its progress. The sensor operational scenario does not necessarily involve dynamic situational analysis, and static images of higher resolution may be appropriate.

Table 7. Comparison of common streaming video compression methods.

	MPEG-1	MPEG-2	H.263
Target bit rate	1.5 Mbit/sec	15 Mbit/sec	64, 128, 192 Kbs up to approx. 2 Mbit/sec
Supported frame rates	25/30 fps	25/30 fps	Any, up to 30 fps
Maximum resolution	320 x 288	720 x 480	352 x 288

A preferred method of visual documentation is to use a still high-resolution digital imaging system. Availability of such systems has been burgeoning in the past few years due to breakthroughs in sensor and storage design. Analysis shows that a typical 1.2 Megapixel image that provides 1 meter per pixel resolution of the terrain can be reduced in size to approximately 100 Kb for color and 50 Kb for grayscale using JPEG compression without significant loss of quality. Other benefits of still imaging include high image quality and native compatibility with Geographic Information System (GIS).

To provide continuous coverage of the terrain with still digital images it is necessary to acquire one image every two seconds (for a 1-m per pixel resolution at 300 meters altitude at the speed

of 100 mph). Transmission of this data will require a channel with minimum throughput of 25-50 Kbs depending on whether color imaging is needed or grayscale photo is sufficient.

3.5.2 Low-Level Networking. Methods of Wireless Communication.

The very principal of remote airborne sensor requires un-tethered (wireless) approach to communications between the sensor and the operator. Numerous standards and principles are currently being developed and established in the area of wireless communications. Most practical and solid approach is based on extending an IP-based design into the area of wireless communications. Advantage of IP-routing vs. proprietary design is in routing flexibility, efficiency and robustness, eased interoperability with Internet and independence of physical media. The intent is the same as the original concept of the Internet: to develop a homogeneous networking capability over a heterogeneous networking infrastructure. Most advances and mature developing standard in area of IP wireless networking is known as Mobile Ad-hoc Networking (MANET). An ad-hoc (or "spontaneous") network is a small network with wireless connections, in which some of the network devices are part of the network only for the duration of a communications session or while in some close proximity to the rest of the network. MANET is a network of highly mobile platforms that are not dependent on pre-existing or fixed communication infrastructure. MANET does not specify any one single physical standard of communication (since wireless technologies will continue to evolve), but rather states that multiple technologies can be used and provides standards-based approach at the network layer.

While wireless technologies continue to rapidly evolve and improve with improvements in both bandwidth and operational range, representative data from mobile router (NovaRoam ED900™ from Nova Engineering) can be used to provide estimations. While more robust wireless high speed solutions with longer range are available, choices for MSLS system are limited due to weight/size constraints of the sensor system. NovaRoam ED900™ fits within those limitations (Table 8) while providing adequate range and bandwidth of communication (Table 9).

Table 8. Specifications of NovaRoam ED900TM.

Parameter	Specification
Description	Wireless router with embedded TCP/IP Stack
Use	Long-range Stationary or Mobile IP-based data communications network (i.e. Internet)
Frequency band	902 - 928 MHz per FCC Part 15 (ISM license-free band)
MANET algorithm	AODV
Network structure	Point-to-point, Point-to-multipoint, Multihop, Mesh
Maximum velocity of mobile nodes	200 MPH (theoretical) - tested at 70 MPH
Dimensions	4.1" x 9.5" x 1.5"
Weight	1.9 lbs
Operating temperature	0 C to +50 C (extended temperature version available)
Storage temperature	-40 C to +85 C
Power input	+10 to +18 VDC or 12 VAC
Power consumption	18 W
Antenna connection	Reverse TNC (due to FCC ISM license-free band)

Table 9. Performance of NovaRoam ED900TM.

Burst data rate (user programmable)	159 kbps	317 kbps	655 kbps	1.008 Mbps
Estimated range (typical, LOS)	10+ miles	8 miles	5 miles	3 miles

Data transmission using MANET network approach via air-to-air or air-to ground communication equipment provides adequate bandwidth for both chemical sensor data and imaging information. However, this method has certain limitations on communication length and is usually confined to distances under 40 miles and for some types of equipment requires transmitter and receiver be in the Line of Sight (LOS). In order to improve operating range of the system and to increase robustness of communications alternative communication channel is suggested.

Satellite communication system is another possible alternative for wireless data exchange. It is being used more extensively by both military and commercial companies. Such systems provide

up to 50 Mb/s bandwidth in Ku-band. However, analyses of systems shows that they do not meet size-weight and power consumption requirements (Table 10) of compact airborne sensor. They require bulky three axis active parabolic antennas and high-power consuming transmitters, which rules out use of such devices in a compact lidar sensor.

Table 10. Specifications of satellite module for ICS by Level 3 communications.

	L"	W"	H"	Weight (lbs)	Power (Watts)
SATCOM Transceiver	16.2	10.4	11.9	26	78
SATCOM Antenna	54.6	48.8	48.8	46	35

Low-speed communication via low earth orbiting (LEO) satellites systems similar to Iridium-9505 terminal can provide alternative mode of wireless communications for the compact airborne lidar. These devices are extremely compact and light-weight (Table 11), and are capable of providing connections with speed of 10 Kb/s. While this speed is not sufficient for digital images transmission, it will still allow to receive vital data from chemical sensor and to send control signals for the airborne sensor. Currently Iridium is working with Department of Defense (DOD) on an Enhanced Mobile Satellite Services (EMSS) program. EMSS is an emerging technology with capability to support low rate data services from a mobile, lightweight terminal. EMSS services will be commercially provided with a few modifications necessary to allow for unique DoD features, such as end-to-end encryption and protection of sensitive user information.

Table 11. Specifications of Iridium 9505 satellite terminal.

	L (mm)	W (mm)	H (mm)	Weight (g)
Iridium 9505 terminal	158	62	59	375

The foregoing analysis of wireless communication methods for the compact mid-IR lidar sensor leads us to propose the following approach. The sensor will have two separate channels of data exchange between the sensor and the command center. The main channel will be based on the 900-MHz band and will be limited to a maximum range of 10 miles. This channel will be responsible for the primary high-bandwidth data transmission. A secondary channel will be based on satellite communications in 1620 MHz band (L-band) and will provide low-bandwidth communications in case LOS channel is not available or impractical to use. The corresponding system architecture is illustrated in Figure 15.

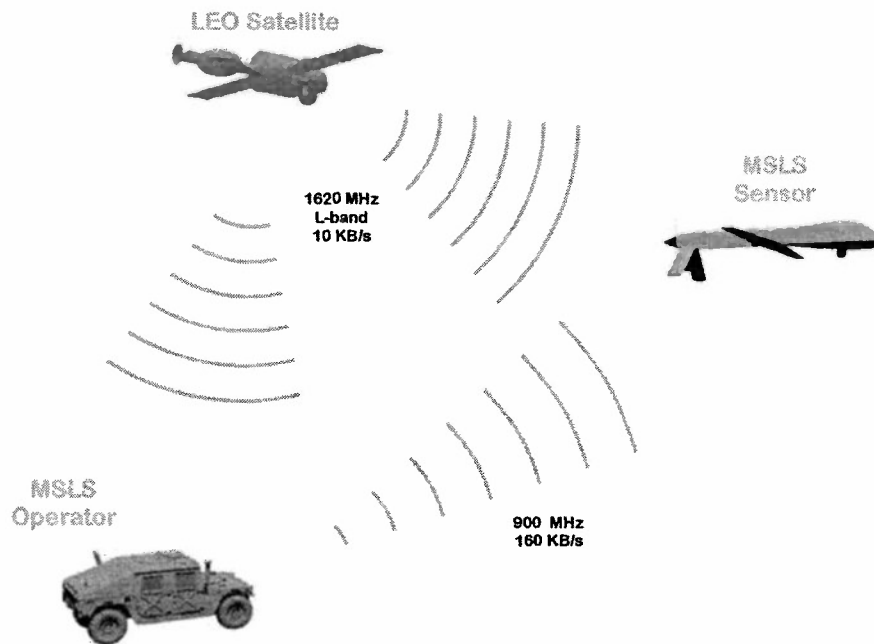


Figure 15. Communications architecture for airborne lidar

3.5.3 High-Level Network and Software Architecture

The compact airborne lidar data reporting network encompasses the sensor itself, a server, operator's console and any number of data review stations (Fig. 16). All nodes of the network are connected to each other through a secure Internet connection with data encryption. Data from the sensor is being exchanged exclusively with the server, which is combined with the operator's console and is also connected to a broadband Internet link. The server handles all requests from data review stations. The server and operator's console may be physically located in a mobile ground command center, airborne unit or in a stationary command post. Wired or wireless high-speed Internet connection is available for all scenarios since operator's console does not have to comply with the same strict weight/size restriction as the sensor itself.

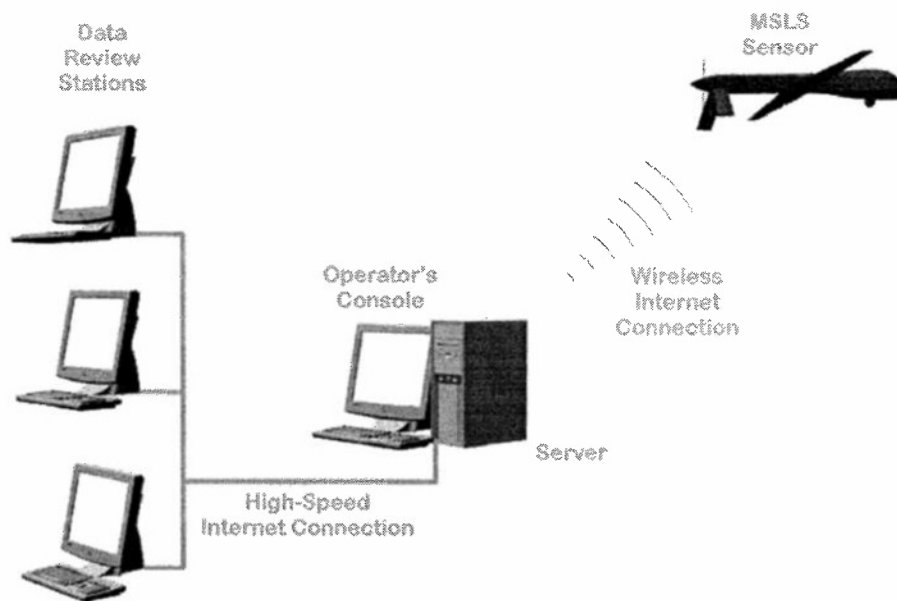


Figure 16. Compact airborne lidar network structure.

At the core of the lidar software is the Geographic Information System (GIS) database. GIS software provides the functions and tools needed to store, analyze, and display data related to locations. It encompasses geographical data such as topographical maps, satellite and aerial photographs organized by their global coordinates. Built-in tools for statistical analyses will enable examination of information collected by the sensor both in spatial and temporal domains. Leading GIS software packages such as MapInfo Professional for Microsoft SQL Server not only contain vast amount of geographical data from maps and photographs to digital elevation models (DEMs), but also are fully customizable which facilitates integration of the lidar data into GIS database. GIS systems are naturally oriented towards Internet use for data exchange and review. GIS database software resides on the lidar server and will handle both dynamic data acquisition from the sensor as well as data requests from the review stations for quasi-real-time data review. This will allow system operator as well as data monitors to dynamically create custom reports that will include chemical information, GPS data, digital images from the sensor and any other information that can be provided by the GIS database (Fig. 17).

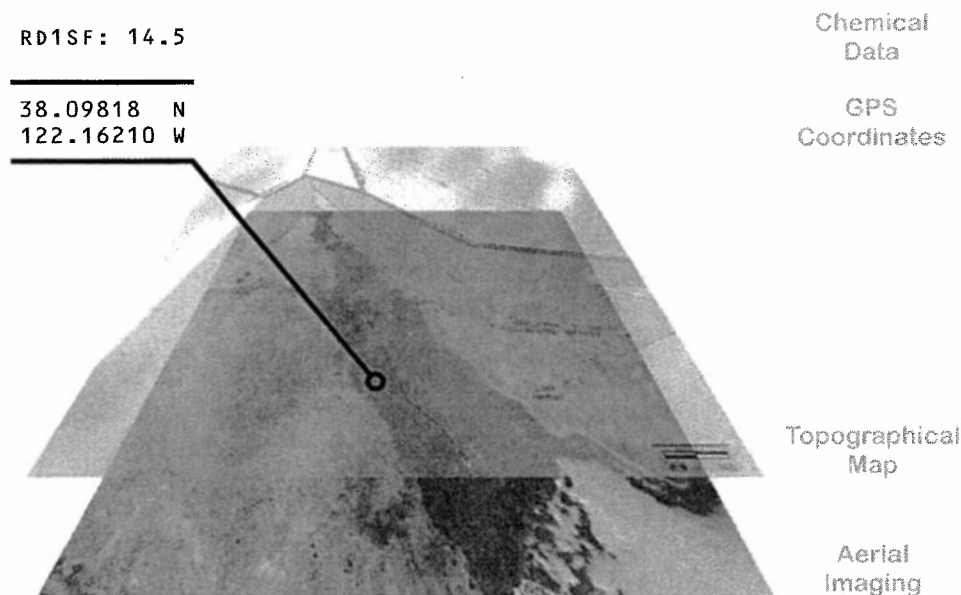


Figure 17. Sample report demonstrating layered presentation of various types of data by GIS software.

3.6 System Testing, Calibration and Verification

The assembled prototype of the compact mid-IR lidar was subjected to extensive ground-based and airborne testing. The main testing objectives were: 1) to ensure a synergistic operation of all system components and sub-systems, 2) to verify airworthiness of the system, 3) to demonstrate chemical detection from an airborne platform, and 4) to establish detection sensitivity limits for various chemicals.

3.6.1 System Spectral Calibration:

Spectral calibration of the system was accomplished by scanning the infrared laser source across its tuning range and recording the signal transmitted through a calibration methane cell. A typical calibration scan is shown in Figure 18. Since the absolute positions of methane lines are well known and tabulated, this method allows one to perform a polynomial approximation of the output wavelength versus tuner position (Fig. 19). Once the spectral calibration is established, any wavelength within the OPO tuning range can be selected by commanding the galvanometer to the corresponding position.

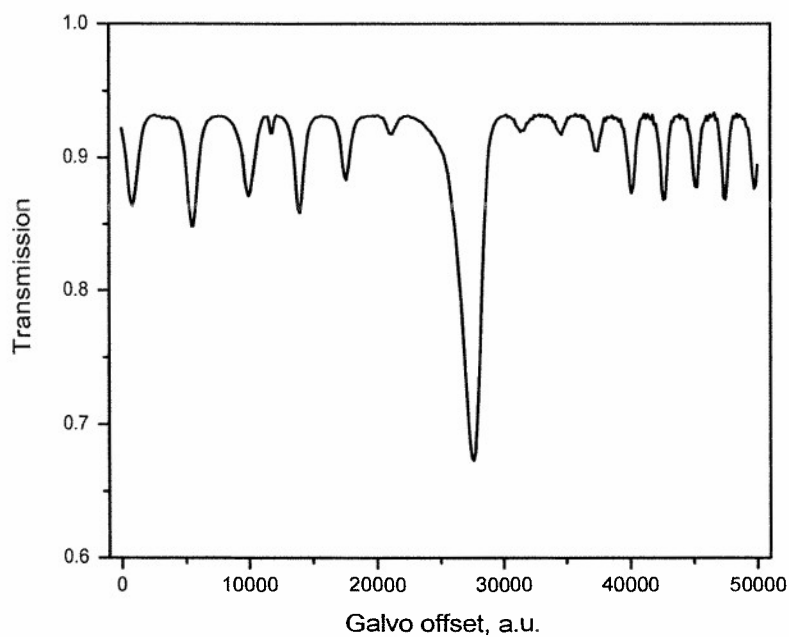


Figure 18. Methane absorption spectrum through a 270 ppm-m absorption cell as a function of raw galvanometer position counts.

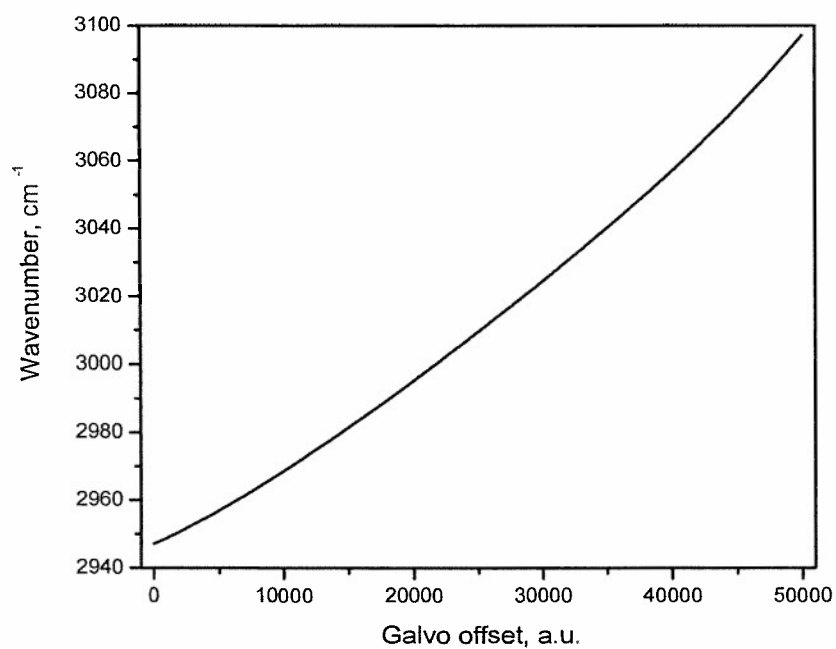


Figure 19. Spectral calibration function.

3.6.2 Ground-based system testing

Ground based testing was accommodated by removing the beam turning mirrors M3 and M4 and propagating the beam along a horizontal path. The propagation path was usually terminated with a rough ground aluminum target which provided a uniform and spectrally flat scattering surface for the reflected beam.

3.6.2.1 Ground-Based Testing: Methane

Methane (CH_4) is a convenient target for active mid-IR sensor testing for two reasons. First, the mid-infrared absorption spectrum of methane is dominated by a number of narrow, well defined peaks (see Figure 18). This makes methane particularly amenable to detection through the differential absorption technique. Second, methane has a background atmospheric level of 1.7 ppm and therefore is readily available for testing. Methane detection capability also has important commercial implications, since this chemical is the major component of natural gas transported through pipelines.

Methane measurement is performed by alternating the laser frequency between two set values. One frequency (the so-called on-line) is coincident with a certain methane absorption line. The other frequency (off-line) is tuned to the wing of the same line. The ratio of the strengths of reflected signals at the on and off lines can be directly related to the path-integrated concentration of methane. This procedure constitutes the classical differential lidar (DIAL) approach to remote chemical measurement.

When choosing the on and off line frequencies, it is important to consider absorption by water vapor. Given the laser source linewidth of 1.2 cm^{-1} , there is a significant overlap of water and methane absorption in the spectral region of laser tuning (Figure 20). The two methane lines that are relatively free from water absorption are the P(7) and Q peaks. Both of these lines were used for DIAL methane measurements. Since the absorption at Q peak is stronger, it generally yields a higher sensitivity compared to the P(7) line.

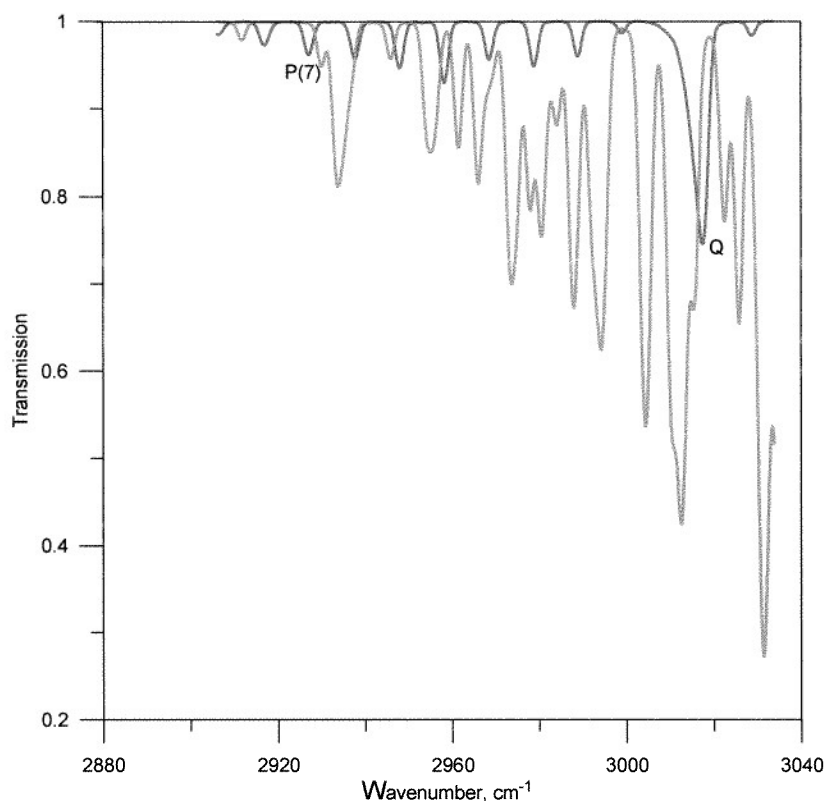


Figure 20. Transmission of a 100-m long path containing 1.7 ppm concentration of methane and 20000 ppm concentration of water.

Ground based methane testing was primarily focused on establishing the system's minimum detectable concentration limit. The latter parameter is determined by noise inherent in the measurement of the on-line to off-line ratio. The key factors contributing to the residual noise level are: noise floor of the pyroelectric and cryo-cooled energy detectors, laser speckle noise, differential albedo noise (for moving targets), spectral interference noise. These noise sources have been discussed at length in literature on differential absorption lidars. It is of interest to see what the net total of these noise contributions is for the specific system and measurement conditions.

In numerous experiments using a stationary retro-reflector, the residual noise of ratio measurement had the standard deviation of $\sigma = 0.002$. The effective differential absorption coefficient corresponding to the Q peak was measured at $\kappa = 7.4 \times 10^{-4} \text{ (ppm-m)}^{-1}$. The equivalent concentration-pathlength uncertainty ΔCL defined as σ / κ is 2.7 ppm-m. Thus, under stationary target conditions, the system is capable low ppm-m level chemical measurement.

3.6.2.2 Ground-Based Testing: Diesel Vehicle Emissions

Diesel emissions associated with running engines can be used to detect concealed military vehicles (e.g., “tanks under trees”). Therefore, diesel fumes represent an important chemical target for an active mid-IR chemical sensor. In order to demonstrate the capability to detect diesel vehicular emissions, we performed an experiment using a commercial diesel powered vehicle.

A Ford F-250 (model year 2000) pickup truck with a diesel engine was left running in the LaSen parking lot in Las Cruces, NM. The site of the demonstration was in a small industrial park east of I-25. Ambient temperature during the test was 52°F, relative humidity R_h was between 45 and 50%, with light winds at 2 to 5 mph.

The mid-IR sensor was operated in a spectral scanning mode in which the laser source was stepped through a sequence of wavelengths from 3.30 μm to 3.42 μm with a line separation of 0.002 μm . The beam path passes directly behind the vehicle's exhaust. A rock wall located approximately 20 meters away served as a topographic reflector.

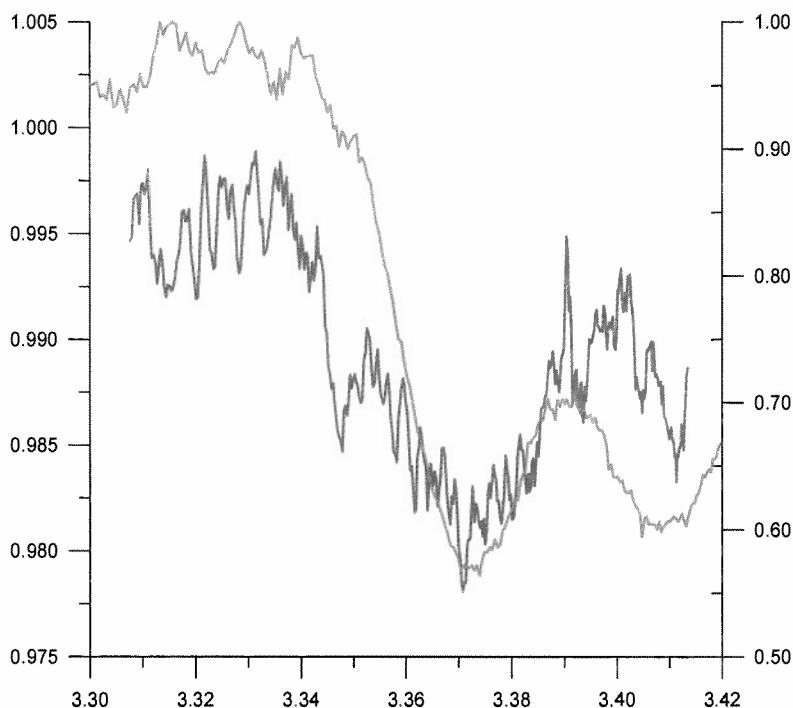


Figure 21. Transmission spectrum of diesel truck emissions (blue) and neat diesel fuel in a calibration cell (red).

Figure 21 shows the transmission spectrum of diesel vehicle emissions (blue line). Atmospheric background due to water and methane has been removed from the spectrum by normalizing it to the spectrum recorded over the same path but with the engine off. Transmission spectrum of neat

diesel fuel in a calibration cell is shown as a reference by the red line. A high degree of correlation between the two spectra is apparent, indicating the presence of diesel fumes in the vehicle emissions. A certain degree of variability in the data is due to plume migration in and out of the beam path caused the wind. It should be noted that the test vehicle was equipped with high altitude emission controls, which makes the ability to detect unburned diesel fuel at such low concentration very encouraging.

3.6.3 Airborne Testing

For airborne testing, a Bell 206 Jet Ranger helicopter was chosen as the sensor platform due to its availability and relative ease of sensor mounting. The sensor is mounted underneath the belly of the helicopter using a modified winch mount standard for Jet Rangers.

Airborne testing involved flying over known and calibrated chemical releases. As an example, consider the results of airborne detection of a methane release at 100 scfh from a partially open pipeline valve. The helicopter carrying the prototype sensor system made 4 passes over the release point. Helicopter position was continuously logged using on-board GPS system. Helicopter path and point of release location are shown on the map in Figure 22.

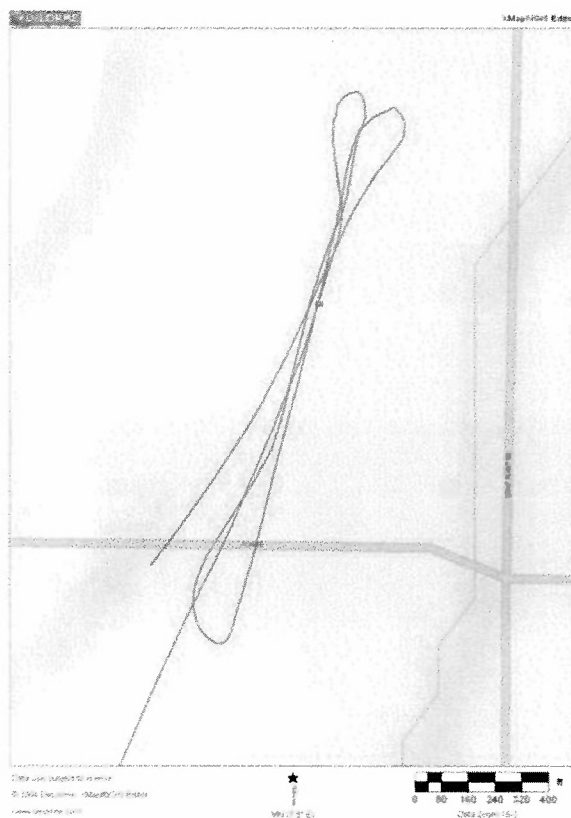


Figure 22. Helicopter flight path superimposed on the area map. A red flag symbol marks the point of methane release.

The differential absorption signal recorded by the system is shown in Figure 23. The four large spikes in the data correspond to the points when the system passed over the methane source. Digital images taken concurrently with the peaks of the differential signal clearly show the release valve. Additionally, infrared images of the methane plume were taken using FLIR Systems GasFindIR infrared camera. Both types of images are shown side by side in Figure 24.

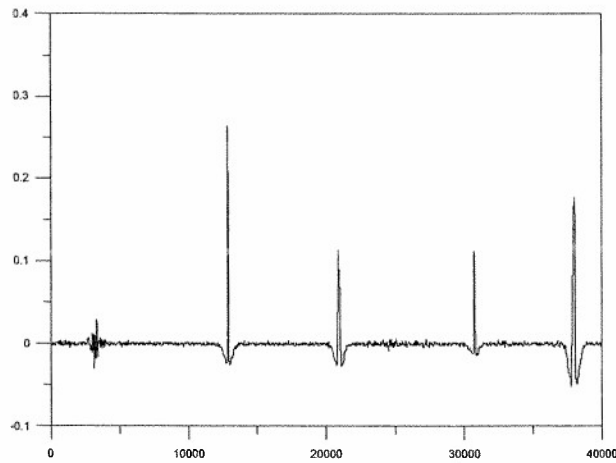


Figure 23. Differential absorption signal in the methane release test. X—pulse number, Y—differential absorption ratio

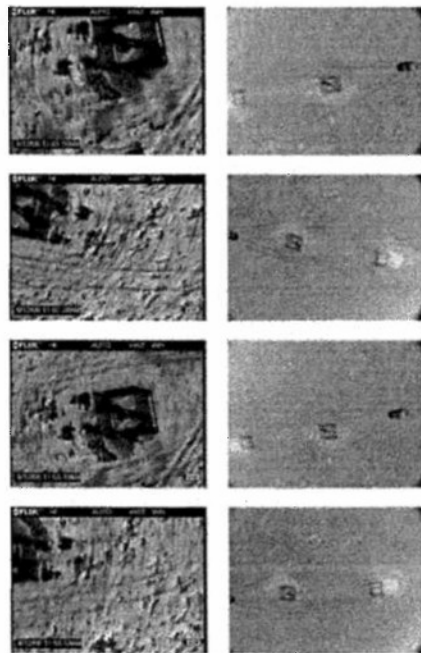


Figure 24. Visual (right) and infrared (left) images of a 100-scfh methane release.

Analysis of data presented in Figures 23 and 24 clearly indicates that the airborne lidar system detected the 100-scfh methane leak on each of the 4 passes. It should be noted that the infrared camera detected the same plume on only 2 out of 4 passes. Thus, a superior sensitivity of an active airborne sensor (lidar) over a passive one (IR camera) is demonstrated.

The high cost of helicopter time (over \$700/hour) and the program's budgetary constraints (\$10,000 allocated for airborne testing) permitted a limited amount of flight time. However, a

wealth of flight performance data is available from the commercial application of LaSen's Airborne Lidar Pipeline Inspection System (ALPIS®) whose design is based on the prototype developed under the DARPA program.

As of this writing, ALPIS has logged in excess of 250 mission hours inspecting over 5000 pipeline miles. The system has stood up extremely well to the rigors of field use and has successfully performed in a wide variety of conditions—from freezing wintry weather to the hot Texas summer. This fact is a testimony to the viability of the design developed under the DARPA program.

3.7 Mid to Near Infrared Up-Conversion Demonstration

3.7.1 Background

In order to successfully discriminate targets in a cluttered environment, such as armored vehicles concealed by foliage, the remote chemical sensor must possess a spatial resolution capability in the sub-meter range. Achieving this level of spatial resolution will require at least an order of magnitude increase in the bandwidth of mid-infrared signal detection over the state-of-the-art technology. A simple estimate of the sensor's spatial resolution, ΔR , can be obtained from the relation: $\Delta R = c(\tau_L + \tau_D)/2$, where τ_D is the detector response time, τ_L is the laser pulsewidth, and c is the velocity of light in free space. Thus, spatial resolution of 1 foot requires the detector response time of 2 ns, provided that the laser pulse width is negligibly small.

The fastest mid-infrared detectors for the 3—5- μm range available on the market today [indium antimonide (InSb) photovoltaic diodes] are limited to approximately 10-MHz bandwidth operation, or greater than 100-ns response time. The major reason for this limitation is the relatively high capacitance of the device (typically, 30 pF and higher). When an InSb photodiode is coupled to a standard transimpedance preamplifier, the dominant noise term for high frequency operation is given by a combination of the detector capacitance and the voltage noise of the preamplifier's input stage. This noise contribution grows as the 1.5 power of the bandwidth, making operation in the hundreds of megahertz range impractical.

The silicon-based detectors, on the other hand, routinely achieve operation with bandwidths of 1 GHz and higher. Additionally, the specific detectivity D^* of silicon photodiodes is roughly two orders of magnitude higher compared to the InSb. However, the spectral response of silicon detectors is limited to 1.1 μm . Therefore, it would be advantageous to convert the incoming infrared signal into the silicon detector range while preserving its temporal characteristics. Such conversion can indeed be achieved by means of nonlinear optics.

The specific process involved is known as the optical parametric up-conversion. The theory and first experimental demonstrations of parametric up-conversion date back to the dawn of nonlinear optics. The merits of up-converters for infrared signal detection were discussed extensively in a large number of publications in the late 1960s – early 1970s [12]. However, since these early studies the interest in parametric up-conversion for signal detection has

diminished. Recent advances in nonlinear crystals, multi-wavelength coatings and compact laser pumping sources have opened up new opportunities for practical design of up-converters. Based on these developments, a significant improvement in size, stability and efficiency of mid-infrared up-converters is possible.

The up-conversion process can be considered as a particular case of optical heterodyne detection. The weak incoming infrared signal is mixed inside a nonlinear optical crystal with a strong field from a local oscillator (pump wave). The pump wave frequency is much higher than the infrared signal frequency and typically lies in the visible to near-infrared spectral range. The result of the mixing process is the emergence of a third wave whose frequency is equal to the sum of frequencies of the pump and infrared waves. It is important to emphasize that the response of the up-converter is instantaneous; in the limit of constant pump intensity, the temporal profiles of the sum-frequency and infrared pulses are identical.

3.7.2 Optical Design of the Up-Converter

Stated in the most basic terms, the function of the up-converter in the compact infrared lidar application is to transform the incoming mid-infrared radiation (3.2—3.6 μm) into the near-infrared (silicon detector) range where it can be detected with a much higher bandwidth and sensitivity. This transformation is accomplished by mixing the incoming signal with an intense pump beam from a local oscillator. The mixing process takes place inside a specially chosen nonlinear optical crystal.

The up-converter module shown in Figure 25 comprises two major sub-components: the pump laser (local oscillator) and the nonlinear crystal. The pump laser exemplifies a standard diode-pumped solid state laser (DPSS) design, except for the somewhat non-traditional *L*-shaped cavity. The laser resonator is formed by the high-reflective (HR) mirror, the input coupler (IC), and the dichroic beamsplitter BS. The HR mirror has maximum reflectivity at the 1064-nm pump wavelength. The input coupler is highly transmissive for the infrared wavelengths, and highly reflective at the pump wavelength. Finally, the dichroic beamsplitter is highly reflective for the *s*-polarized pump wave and is highly transmissive for the *p*-polarized sum-frequency wave. The *L*-shaped cavity layout allows for simple and effective coupling of the infrared radiation into the device and extracting the up-converted signal from the resonator. A short-pass optical filter placed in front of the detector blocks the 1064- μm pump radiation which could otherwise swamp the weak signal.

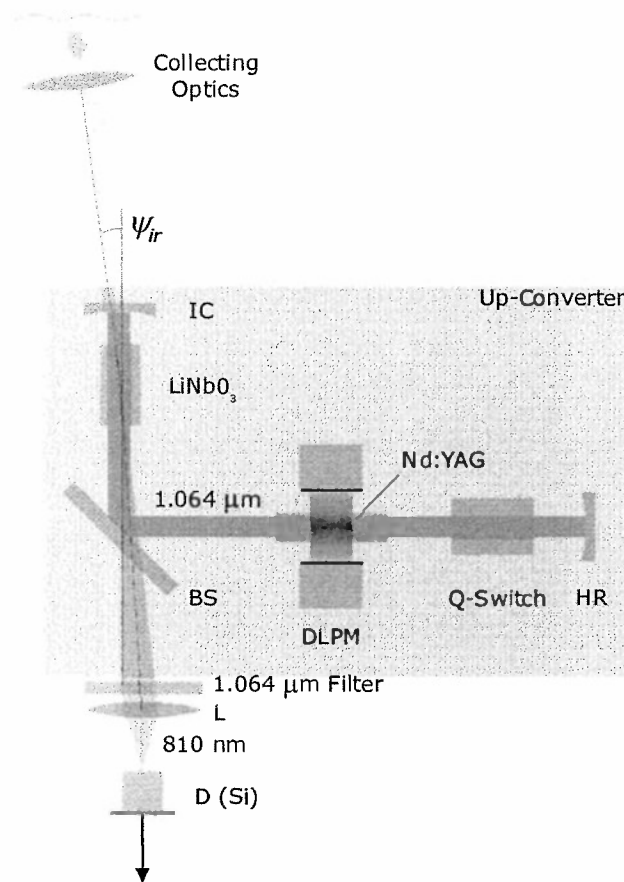


Figure 25. Up-converter optical layout.

The diode pump laser module (DPLM) incorporates a rod of neodymium yttrium garnet (Nd:YAG) material. The rod is radially pumped by several linear arrays of semiconductor laser diodes arranged around the rod in a sleeve-like configuration. The diode pump wavelength is chosen to coincide with the peak absorption of the Nd:YAG material. An electro-optical Q-switch, consisting of a polarizer, a quarter-wave plate and a Pockels' cell is used to produce high intensity, tens-of-nanoseconds-long laser pulses.

A number of nonlinear crystals can be used for the mid-infrared optical up-conversion. Of the available options, lithium niobate (LiNbO_3) was chosen for this particular up-converter implementation. The application of this crystal for mid-infrared up-conversion has been studied extensively. Additionally, lithium niobate crystals are readily available from several manufacturers in exceptionally large sizes and with consistent quality.

The center ray of the incident infrared cone makes an angle ψ_{ir} with the pump beam axis. The reason for this special arrangement will become clear when we consider the solid acceptance angle of the up-converter in Section 3.7.4.

In the following subsections, we present theoretical estimates for the key performance parameters of the up-converter shown in Figure 25.

3.7.3 Conversion Efficiency

The up-conversion efficiency is defined as the ratio of the output power at the sum frequency to the input power at the infrared frequency [13]:

$$\eta = \frac{P_s(L)}{P_{ir}(0)} = \frac{\omega_s}{\omega_{ir}} \kappa^2 L^2 \text{sinc}^2(\Gamma L), \quad (2)$$

where L is the nonlinear crystal length. The gain coefficient Γ is given by

$$\Gamma = \left[\kappa^2 + \left(\frac{\Delta k}{2} \right)^2 \right]^{1/2},$$

$$\kappa^2 = \frac{2\omega_{ir}\omega_s d_{eff}^2 I_p}{n_{ir}n_s n_p \epsilon_0 c^3}.$$

where I_p is the pump beam intensity, d_{eff} is the effective nonlinear coefficient, ϵ_0 is the permittivity of free space, and c is the velocity of light in free space. The parameter Δk is called the wave vector mismatch and is explained in detail in the next subsection. If the efficiency is expressed in terms of photon numbers rather than optical powers, the signal-to-idler frequency ratio in Equation (2) vanishes. Equation (2) implies that the quantum conversion efficiency of an up-converter has a theoretical limit of 100%. However, this statement is only true in the plane-wave approximation when the spatial profile of the interacting waves is not taken into account. Practically achievable conversion efficiency is always lower than the theoretical limit and depends on a number of factors that will be discussed later in this report.

Notwithstanding the last comment, equation (2) provides a reasonable basis for estimating the pump beam intensity required for effective up-conversion. Consider a specific case of up-converting the infrared radiation with $\lambda_{ir} = 3464$ nm by mixing it with in a 1064-nm pump in a lithium niobate crystal. The effective nonlinear coefficient for this interaction is $d_{eff} = 5.8$ pm/V. Substituting these parameters into (2) and assuming negligible phase mismatch ($\Delta k = 0$), we obtain

$$\eta = \frac{\omega_s}{\omega_{ir}} \sin(1.8 \times 10^{-4} \sqrt{I_p} L). \quad (3)$$

As we show in the next section, it is desirable to keep the crystal length short (~ 1 cm) in order to maintain wide spectral and angular acceptance bandwidth for the up-converter. Consequently, the pump beam intensity on the order of 10—100 MW/cm² is required for high conversion efficiency. At this point, the advantage of putting the nonlinear crystal inside the pump laser

cavity becomes apparent. The intra-cavity intensity is typically orders of magnitude higher than the beam intensity external to the cavity for the same beam size. The megawatt intensity levels are easily achievable internal to the cavity when the pump laser is operated in a Q-switched pulsed mode.

Intra-cavity pump intensity can be estimated based on the following relation:

$$I = \frac{E}{\tau \pi \omega_0^2}, \quad (4)$$

where E is the total energy stored in the resonator, τ is the resonator round trip time, and ω_0 is the pump beam radius. In deriving (4) we assumed for simplicity that the pump mode volume can be approximated by a cylinder of radius ω_0 .

Consider a pump resonator that is 15-cm long. Assume further that the total pump energy contained in the cavity is 10 mJ. Equation (4) then yields $I = 10^7 / (\pi \omega_0^2)$. Therefore, the pump beam radius can be on the order of 5 mm to produce the intensity level required for efficient up-conversion.

3.7.4 Up-Converter Solid Acceptance Angle

Practical design parameters for an up-converter can be drastically different depending on whether the input signal is a collimated beam or radiation from an extended source. In a laser-based remote sensor, the up-converter would be located behind an optical system collecting radiation reflected by a remote target. Thus, the up-converter must accept radiation within a relatively wide cone of angles determined by the speed (F-number) of the collecting optical system.

Of critical importance to the performance of an up-converter is the parameter known as the solid acceptance angle. Unlike a conventional detector which can theoretically accept input radiation from a 2π -steradian solid angle, the up-converter is only sensitive to input radiation within a relatively narrow spatial cone called the solid acceptance angle. The restriction on the acceptance angle stems from the requirement to satisfy the phase-matching conditions which we discuss next.

Two fundamental conservation laws govern nonlinear wave interactions. The law of energy conservation mentioned above requires that the sum of the infrared and pump frequencies be equal to the up-converted signal frequency:

$$\omega_{ir} + \omega_p = \omega_s. \quad (5)$$

The law of momentum conservation requires that the vector sum of the infrared and pump wave vectors be equal to the signal wave vector:

$$k_{ir} + k_p = k_s. \quad (6)$$

where

$$k_{ir} = \frac{n_{ir}\omega_{ir}}{c}, k_p = \frac{n_p\omega_p}{c}, k_s = \frac{n_s\omega_s}{c}.$$

In an isotropic optical medium, equations (5) and (6) cannot be satisfied simultaneously because of dispersion, which results in $n_s > n_p > n_{ir}$.

In an anisotropic optical medium such as a nonlinear crystal the refractive index and hence the length of the k vector depend on the direction of propagation and the polarization state of light. It becomes possible to choose a specific direction and polarization state for the three waves to satisfy the energy and momentum conservation relations simultaneously. This process is called the birefringent phase-matching.

If the three wave vectors involved in the parametric interaction are non-collinear, the phase matching process is referred to as vector phase matching. Consider the vector phase-matching geometry shown in Figure 26 which applies to negative uniaxial crystals such as lithium niobate. The optical axis of the crystal c lies in the plane of the drawing. The pump and infrared waves are polarized perpendicular to the plane of the drawing and thereby propagate as ordinary waves. For these waves, the length of the k -vector are independent of the propagation angle. The signal wave, on the other hand, propagates as an extraordinary wave with the polarization vector lying in the plane of the drawing. The tip of the k_s vector traces an ellipse as the angle between the propagation direction and the crystal axis is changed. This particular type of three-wave parametric interaction is referred to as Type I, and is frequently labeled as *ooe*.

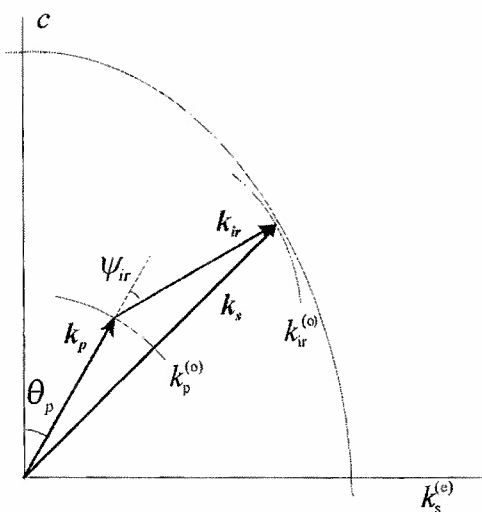


Figure 26. Tangential phase matching geometry in lithium niobate.

Under the exact phase-matching conditions, the vector triangle shown in Figure 26 is closed. If any of the parameters deviate from their values corresponding to the exact phase-matching, a vector mismatch defined as $\Delta k = |\mathbf{k}_s - \mathbf{k}_p - \mathbf{k}_i|$ will result. In the vicinity of the exact phase-matching point, Δk can be expanded in the Taylor series of its parameters:

$$\Delta k = \frac{\partial \Delta k}{\partial \psi_{ir}} \Delta \psi_{ir} + \frac{\partial \Delta k}{\partial \omega_{ir}} \Delta \omega_{ir} + \dots, \quad (7)$$

where only two parameters of interest are shown explicitly and higher order derivative have been neglected. According to equation (2) any vector mismatch results in a decrease of the conversion efficiency. The conversion efficiency is reduced by a factor of two from its maximum value when $\text{sinc}^2(\Gamma L) = 0.5$, or, equivalently:

$$\Gamma L = \left[\left(\frac{\Delta k L}{2} \right)^2 + \kappa^2 L^2 \right]^{1/2} = 1.39156.$$

Neglecting the second term in square brackets, we obtain the expression for wave mismatch corresponding to a factor of two reduction in the conversion efficiency:

$$\Delta k = 0.886\pi L^{-1}. \quad (8)$$

Equations (7) and (8) form the basis for estimating the tolerance of the up-conversion process to variations of the infrared frequency and angle.

Consider first the tolerance on the variation of the infrared angle. This parameter is directly related to the field-of-view of the up-converter. To achieve the widest possible field-of-view one needs to find the conditions under which Δk is minimally sensitive to the variations of ψ_{ir} . It can be shown that the widest tolerance on the infrared angle is achieved when the k -vector surfaces for the sum-frequency and the infrared waves are tangential. This situation is illustrated in Figure 27. In this case, the first derivative of Δk with respect to the infrared angle in Equation (7) vanishes, and one needs to consider the second derivative term proportional to $\Delta \psi_{ir}$ squared. Note that the tangential phase-matching condition requires that the infrared and pump waves be non-collinear. The specific angles ψ_{ir} and θ_p depend on the infrared wavelength.

To obtain a qualitative estimate of the field-of-view under tangential phase-matching conditions, we need to express Δk as a function of ψ_{ir} . Then, the condition (8) can be used to define the acceptance range for the infrared angle. By definition, at the end-points of the acceptance range the conversion efficiency is reduced in half. Although it is possible to obtain an analytical expression for $\Delta \psi_{ir}$ (see Ref. [12] for details), we find a numerical approach to be more convenient. Figure 2.3 shows Δk as a numerically computed function of the infrared angle deviation in a 1-cm long LiNbO₃ crystal. The internal field-of-view half angle is approximately 14 mRad. Multiplying the internal angle by the refractive index of LiNbO₃ at 3.464 μm gives the external field-of-view (full angle) of 56 mRad. This relatively narrow field-of-view is adequate, and perhaps even desirable for long-range detection applications.

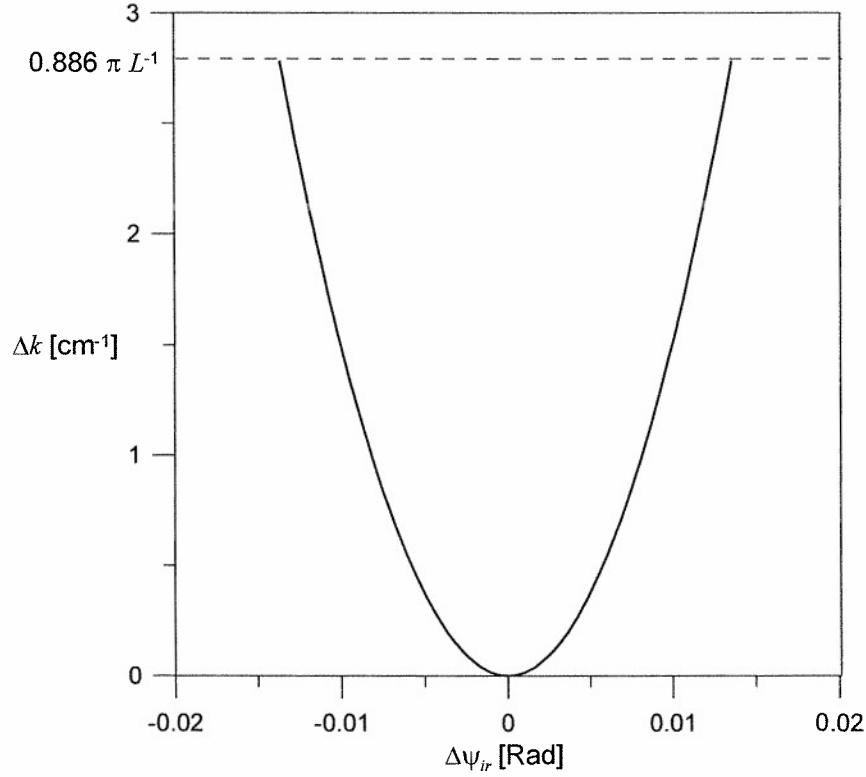


Figure 27. Phase mismatch as a function of the infrared angle deviation.

The solid acceptance angle of the up-converters is: $\Omega = \pi (n_{ir} \Delta\psi_{ir})^2$. Together with the pump beam size through the nonlinear crystal, the acceptance angle Ω determines the étendue of the device.

According to (8) the field-of-view of an up-converter is inversely proportional to the crystal length L . On the other hand, the conversion efficiency can increase with L . Therefore, there is a tradeoff between the up-converter field-of-view and efficiency.

3.7.5 Up-Converter Spectral Acceptance Bandwidth

In this section we consider the limits on the up-converter spectral acceptance bandwidth $\Delta\omega_{ir}$. Once again, we are interested in the conditions under which this parameter is maximized. The reason for maximizing the spectral bandwidth is that the up-converter will be working in a tandem with a tunable laser source. Therefore, the up-converter must have high sensitivity across the entire tuning band of the laser source, typically from 3.2 to 3.6 μm .

The same argument used in the previous section to achieve the largest solid acceptance angle applies to the spectral bandwidth. The widest acceptance bandwidth corresponds to the point where the first derivative of Δk with respect to ω_{ir} vanishes. This point is called the dispersion phase-matching point. For the Type I phase-matching in lithium niobate pumped with Nd:YAG laser pump, the dispersion phase matching point corresponds to $\lambda_{ir} = 3.464 \mu\text{m}$. Spectral acceptance bandwidth under dispersion phase-matching conditions in lithium niobate is shown in Figure 28. The crystal is assumed to be 1-cm long.

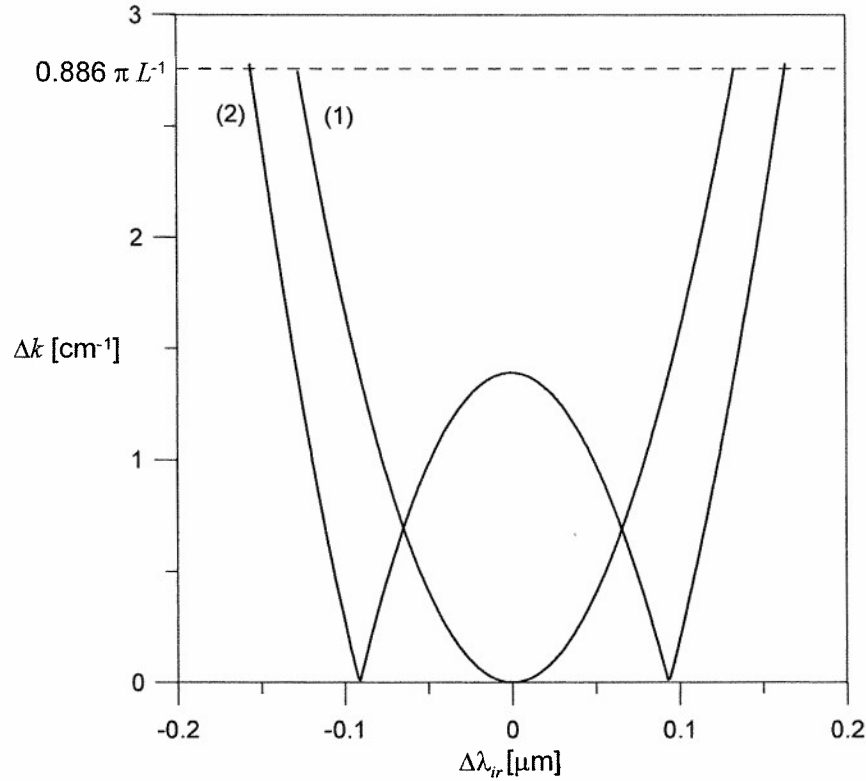


Figure 28. Spectral acceptance bandwidth of a lithium niobate up-converter.

Spectral acceptance bandwidth of the up-converter can be further increase by allowing a phase mismatch at the center frequency of the infrared band. This situation is illustrated by curve (2) in Figure 28. Results shown in Figure 28 indicate that under dispersion phase matching conditions the spectral acceptance bandwidth of a lithium niobate up-converter can exceed 300 cm^{-1} , which should be sufficient to cover the full tuning band of the laser source.

3.7.6 Pulsed Mid-IR Optical Up-Converter Experiments

To verify conclusions of theoretical analyses presented in the previous sections, an intracavity optical parametric up-converter test bed was assembled and experimentally investigated. This section presents the results of up-conversion experiments with a black body emitter serving as an IR radiation source.

3.7.6.1 Experimental Setup

The up-converter module was assembled on a small optical breadboard. Experimental layout is shown in Figure 29. The 90% reflector is a concave mirror with a 5-m radius of curvature. This optic is a standard CVI part (Y1-1025-0-5.00CC). The input coupler is a plano-plano optic and is another standard CVI part (OPOM-0-R1064-T3200-3700-PM). The dichroic beamsplitter is custom made by VLOC.

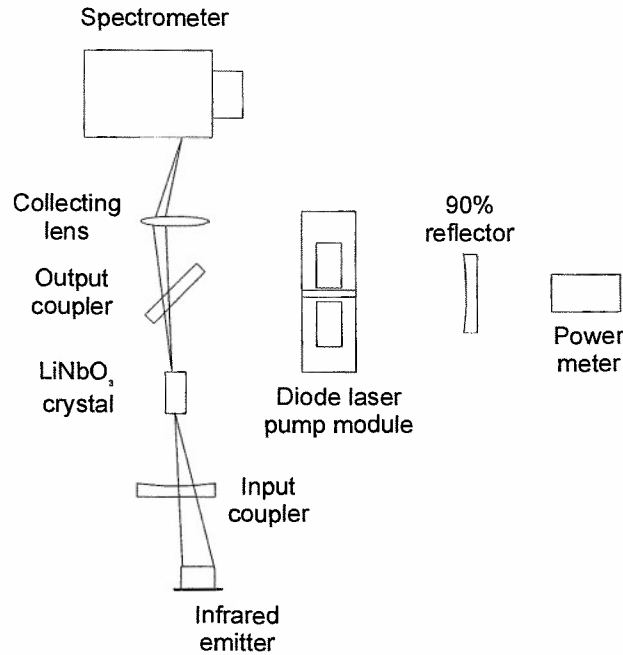


Figure 29. Optical layout of the up-conversion experiment.

The lithium niobate crystals used in the up-converter module were procured from Deltronic Crystals, Inc. All crystals were cut at $\theta = 45^\circ$ for dispersion phase matching, and $\varphi = 30^\circ$ or $\varphi = -90^\circ$ for maximum nonlinear efficiency. Crystals of two different sizes ($5 \times 5 \times 10$ mm and $5 \times 5 \times 15$ mm) were used to investigate the tradeoff between conversion efficiency and solid

acceptance angle. The crystals were coated by VLOC to ensure low insertion loss for the 1.064- μm pump wavelength, and low losses for the IR and signal radiation. Two opposite long surfaces of each crystal have Cr:Au electrodes deposited upon them for electro-optical tuning. For mounting the nonlinear crystal, a customized version of DPI crystal holder was procured. The DPI mount has high mechanical stability, rigid angular adjustments, and built in electrical leads for applying high voltage to the crystal. Prior to installation into the mount, all lithium niobate crystals were initially characterized to determine the direction of the c -axis. The opto-mechanical layout of the up-converter is shown in Figure 30.

The IR source fills up the entire field-of-view of the nonlinear crystal. Cal Sensors miniature IR emitters were used as a blackbody source for setting the operation point of the up-converter. Model SA 10510 emitter is capable of handling up to 3 W of input power and is packaged in a TO-8 size can. The output aperture of the crystal is imaged onto the slit of the CP200 spectrometer with intensified diode array. After aligning the 1.064- μm cavity, pump energies close to 15 mJ per pulse were measured through the 90% output coupler. With the pump laser on, the acquired spectra had prominent peaks at 532 nm, corresponding to the second harmonic of Nd:YAG, and in the 810 to 900-nm region, corresponding to the diode pump and Nd:YAG fluorescence wavelengths. This radiation propagates co-linearly with the pump beam and is highly directional. Most of it can be effectively blocked by moving an opaque screen into the pump beam path next to the collecting lens. The screen does not affect the up-converted signal, as this radiation propagates at an angle to the pump beam.

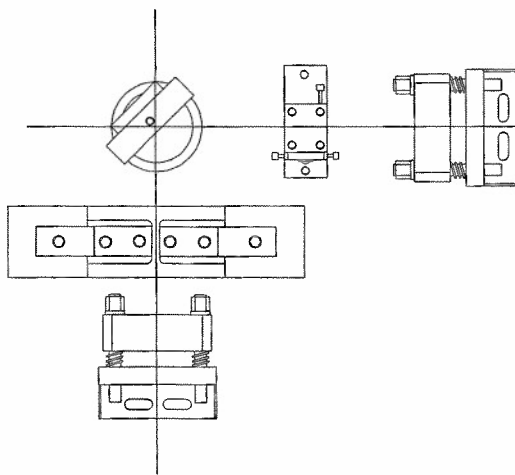


Figure 30. Up-converter mechanical layout.

3.7.6.2 Black Body Up-Conversion Tests

The main objective at this stage was to obtain a tunable up-conversion of a black-body source. The situation was complicated by the fact that the operation wavelength of the laser diodes used to pump the Nd:YAG rod (810 nm) coincides with the center of the up-conversion signal band

for the LiNbO_3 crystal. Given the extremely high brightness of the laser diode source (up to 600 W quasi-cw), the up-converted signal can easily get drowned in the background.

Several steps were taken to decrease the amount of laser diode light at the spectrometer. An extensive array of optical screens and baffles was employed to minimize the amount of the diffuse 810-nm light. Additionally, a dichroic beamsplitter was inserted into one leg of the cavity that transmitted the 1064-nm radiation and reflected the 810 nm at 45° incidence. Finally, a different collecting optics layout was employed. Instead of imaging the exit surface of the crystal onto the entrance slit of the spectrometer, a non-imaging collecting lens was used. This lens transformed the angles of inclination for rays exiting the nonlinear crystal into displacements from the optical axis in the plane of the slit. The up-converted signal cone has a narrow angular spread, and its center ray makes an angle of approximately 1.4 degrees with the optical axis. Thus, by adjusting the position of a narrow (0.25 mm) spectrometer slit it was possible to find a position of the slit where the signal intensity was high, and the interfering contribution from laser diodes considerably reduced.

With the above improvements, a tunable up-converted signal was observed with a good signal-to-noise ratio (Figure 31). Tuning was accomplished by rotating the crystal. The theoretical analysis of up-conversion in LiNbO_3 crystal predicts two peaks symmetrically located with respect to the center wavelength of 810 nm. Only one of these peaks (on the short-wave side) was experimentally observed. This discrepancy is attributed to the spectral response of the photocathode of the intensified detector array which falls off sharply around 810–820 nm.

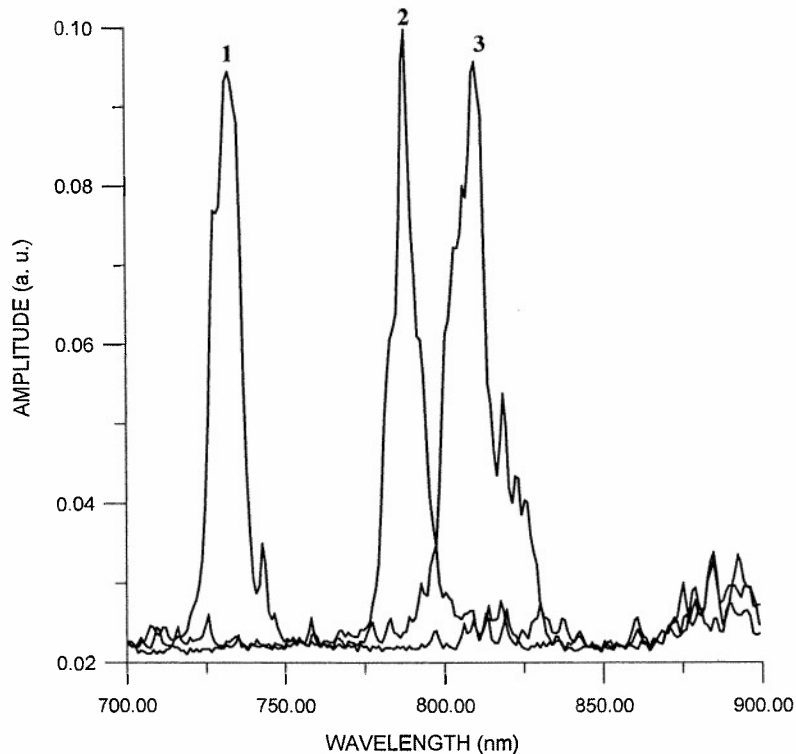


Figure 31. Spectral tuning of up-converted radiation from a black body source. The pump beam external angle is θ . (1) $\theta = 11^\circ$, (2) $\theta = 5^\circ$, (3) $\theta = 4^\circ$.

4 Conclusions

A prototype compact mid-infrared airborne lidar for remote chemical detection has been designed, assembled and tested. The design based on the state-of-the-art technologies has resulted in a compact and lightweight sensor package. However, the prototype's weight and size parameters still significantly exceed specifications desired for deployment on small UAVs.

Further reduction of the sensor's weight and size hinges on the availability of more efficient laser sources for the mid-IR. It appears unlikely that the efficiency of OPO-based systems can be improved much further. Hence the weight, size and power overhead will remain relatively constant. High power infrared semiconductor lasers promise a much higher conversion efficiency and should result in further improved transmitters for future mid-IR lidar systems.

Frequency agility at pulse repetition rates up to 100 Hz is readily achieved with OPO-based mid-IR laser sources. A fast and accurate angular tuning can be achieved by mounting the nonlinear crystal to the shaft of a closed loop galvanometric scanner which is operated in a step-and-settle or sinusoidal mode.

Operation from a long standoff range will require a line narrowed laser source to enable "seeing" between water and methane absorption lines. Using the natural linewidth of a type-II OPO leads to 1-cm^{-1} laser linewidth which results in spectral smoothing and component mixing. For shorter operation ranges and selected chemicals, this limitation can be overcome by a judicious choice of operating wavelengths.

The up-conversion technique is best suited for detection of single-mode infrared signals. Its usefulness for lidar signal detection is limited due to the inherently small étendue, which stems from the phase matching conditions of the nonlinear optical up-conversion process.

References

1. André G. Lareau, "Tactical Airborne Reconnaissance Goes Dual-Band and Beyond," *Photonics Spectra*, **July**, 64 (2002).
2. Air Force Web site:
http://www.af.mil/news/factsheets/RQ_1_Predator_Unmanned_Aerial.html
3. NASA Unmanned Aerial Vehicle Web Site: <http://uav.wff.nasa.gov/>
4. R.S. Conroy, C.F. Rae, M.H. Dunn, B.S. Sinclair, J.M. Ley, "Compact, actively Q-switched optical parametric oscillator," *Opt. Lett.* **24**, 1614 (1999).
5. R.F. Wu, K.S. Lai, H.F. Wong, W.J. Xie, Y.L. Lim, E. Lau, "Multiwatt mid-IR output from Nd:YALO laser pumped intracavity KTA OPO," *Optics Express* **8**, 694 (2001).
6. R.J. Green, K. Chinn, R. Saunders, L.N. Cater, B. Rowland, "Agent/simulant performance correlation," in *Proceeding of 5th Joint Conference on Standoff Detection for Chemical and Biological Defense* (Sept. 2001).
7. W.M. Pfenninger and F. Magnotta, "Frequency-agile MWIR lidar results from Aberdeen proving ground biosimulant releases," Final Report, November 1999.
8. D.L. Fenimore, K.L. Shepler, U.B. Ramabadran, S.R. McPherson, *J. Opt. Soc. Am. B.* **12**, 794 (1995).
9. S.T. Yang and S.P. Velsko, Frequency-agile kilohertz repetition-rate optical parametric oscillator based on periodically pooled lithium niobate, *Opt. Lett.* **24**, 133 (1999).
10. K. Akagawa, S. Wada, and H. Tashiro, High-speed optical parametric oscillator pumped with an electronically tuned Ti:sapphire laser, *Appl. Phys. Lett.* **70**, 1212 (1997).
11. M.E. Klein, P. Gross, K.-J. Boller, M. Auerbach, P. Wessels, C. Fallnich, Rapidly tunable continuous-wave optical parametric oscillator pumped by a fiber laser, *Opt. Lett.* **28**, 920 (2003).
12. J. Warner, Difference frequency generation and up-conversion, in *Quantum Electronics: a Treatise*, H. Rabin and C.L. Tang, eds., Academic Press, NY (1975).
13. Yariv, *Quantum Electronics*, (John Wiley & Sons, 1989), 427.